Inhibition of HIV infection by structural proteins of the inner nuclear membrane is associated with reduced chromatin dynamics

Anvita Bhargava[1], Mathieu Maurin[1], Patricia Davidson[2], Mabel Jouve[1], Xavier Lahaye[1,#], Nicolas Manel[1,#]

[1] Institut Curie, PSL Research University, INSERM U932, Paris, France.

[2] Laboratoire Physico-Chimie Curie, Institut Curie, CNRS UMR168, Sorbonne Université, PSL Research University, Paris, France.

Correspondance : nicolas.manel@curie.fr

# Equal contribution

Abstract

The Human Immunodeficiency Virus (HIV) enters the nucleus to establish infection. The nuclear envelope is a physical barrier for HIV. The role of nuclear pore components in promoting HIV infection is well established. In contrast, the role of other proteins of the nuclear envelope is much less understood. SUN1 and SUN2 are inner nuclear membrane proteins that connect the nuclear Lamin proteins to the cytoskeleton. Increased levels of SUN1 or SUN2 proteins potently restrict HIV infection through an unresolved mechanism. Here, we identify a strain-specific antiviral activity of SUN1 and SUN2 against HIV-1 and HIV-2 that we leverage to investigate the cellular basis of the antiviral effect. SUN1 preferentially restricts HIV-1 in macrophages and HeLa cells. This specificity maps to the nucleoplasmic domain of SUN proteins, which associates with Lamin A/C and participates to the DNA damage response. We find that etoposide, a DNA-damaging drug, stimulates infection. Inhibition of ATR, which induces a DNA damage response, also enhances HIV-1 infection. The proviral effect of ATR inhibition on infection requires the Vpr gene in HIV-1. Depletion of endogenous Lamin A/C, which sensitize cells to DNA damage, also enhances HIV-1 infection in HeLa cells. SUN1 over-expression neutralizes these proviral effects, while the antiviral effect of SUN2 is rescued by etoposide treatment. Finally, we show that inhibition of HIV-1 infection by over-expressed SUN proteins and endogenous Lamin A/C is associated with reduced internal movements of chromatin and reduced rotations of the nucleus. Altogether, the results highlight distinct antiviral activities of SUN1 and SUN2 and they reveal an emerging role of nuclear movements and the DNA damage response in the control of HIV infection by structural components of the nuclear envelope.

41 **Introduction**

42 Successful infection of cells by HIV requires that the virus actively passes through the physical
43 barrier of the nuclear envelope. Nuclear entry of HIV is coordinated with completion of reverse
44 transcription and selection of integration sites (Dharan et al., 2020; Schaller et al., 2011). The
45 capsid protein of HIV engages multiple interactions with nuclear pore complex (NPC)
46 components and associated proteins such as Cyclophilin A to achieve this coordination
47 (Yamashita and Engelman, 2017).

48 In the nuclear envelope, in addition to NPC proteins, SUN proteins located in the inner nuclear
49 membrane of nucleus impact HIV infection (Bhargava et al., 2018). SUN1 and SUN2 are
50 integral proteins of the inner nuclear envelope of somatic cells. They play essential roles in the
51 maintenance of genomic stability and the resolution of DNA damage (Lawrence et al., 2016;
52 Lei et al., 2012). SUN proteins possess a Lamin-binding domain at their N-terminus located in
53 the nucleoplasm. Lamins are intermediated filament proteins that assemble the nuclear lamina,
54 a dense meshwork contributing to mechanical protection, organization of chromatin domains
55 and recruitment of DNA repair factors (Burke and Stewart, 2013; Gonzalo, 2014). At their C-
56 terminus, SUN proteins interact with Nesprins in the perinuclear space. Nesprins are large
57 integral proteins of the outer nuclear membrane (Burke and Stewart, 2013). Nesprins have
58 multiple interactions with cytoskeletal proteins, enabling a dynamic anchoring of the nucleus
59 within the cells.

60 SUN2 was first identified as an antiviral factor against HIV-1 in the context of a cDNA screen
61 (Schoggins et al., 2011). Subsequent studies confirmed and extended the antiviral viral effect
62 of SUN1 and SUN2 over-expression on HIV-1 and HIV-2 infection (Donahue et al., 2016;
63 Lahaye et al., 2016; Luo et al., 2018; Schaller et al., 2017). SUN1 and SUN2 over-expression
64 limits the level of HIV-1 nuclear import as assessed by 2-LTR circles levels in U87MG, CHME
65 and HEK293A cells (Donahue et al., 2016; Luo et al., 2018; Schaller et al., 2017), leading to

66 reduced viral integration. Nanotubes of HIV-1 capsid and nucleocapsid proteins produced *in*
67 *vitro* pull down SUN1 and SUN2 proteins from cell lysates (Schaller et al., 2017).
68 The role of endogenous SUN2 in HIV-1 infection has been examined in several studies but this
69 has not reached a consensus (Donahue et al., 2017; Lahaye et al., 2016; Schaller et al., 2017;
70 Sun et al., 2018). Three studies concurred with a requirement for SUN2 in HIV-1 infection in
71 primary CD4+ T cells, in monocyte-derived dendritic cells and in THP-1 cells, although the
72 strength of this requirement varies between cell type (Donahue et al., 2017; Lahaye et al., 2016;
73 Schaller et al., 2017). A fourth study obtained contradicting results and proposed that
74 endogenous SUN2 instead limits HIV infection at the level of LTR expression (Sun et al.,
75 2018). SUN2 is also implicated in the effects of Cyclophilin A (CypA) on HIV-1 infection. In
76 HeLa cells, SUN2 over-expression abrogates the sensitivity of HIV-1 capsid mutant N74D to
77 Cyclophilin A inhibition (Lahaye et al., 2016). In primary CD4+ T cells and murine bone-
78 marrow derived dendritic cells, one study found that endogenous SUN2 is required for the
79 Cyclophilin A-dependent steps of HIV infection (Lahaye et al., 2016), while another study did
80 not observe this effect in primary CD4+ T cells (Donahue et al., 2017). We initially proposed
81 that HIV depends on a sweet-spot of SUN2 protein expression (hormesis), and that too little or
82 too much expression impairs infection, not necessarily through the same mechanism (Lahaye
83 et al., 2016). This notion fits well with the structural role of the LINC complex in nuclear
84 architecture. Noteworthily, endogenous SUN2 level varies with the extent of T cell activation
85 (Sun et al., 2018). It is thus conceivable that variable experimental conditions between studies,
86 particularly using sensitive primary immune cells, could account for the variable effects of
87 endogenous SUN2 on HIV infection. Our understanding of the antiviral effect of SUN1 is less
88 advanced. In HEK293A cells, the antiviral effect of SUN1 over-expression requires Cyclophilin
89 A interaction with HIV-1 capsid protein (Luo et al., 2018). In THP-1 cells, endogenous SUN1
90 is not required for HIV-1 infection (Schaller et al., 2017).

91 The strong antiviral effect of SUN protein over-expression on HIV infection exploits one or
92 several points of weakness in the viral replication cycle. The cellular mechanisms by which
93 elevated levels of SUN protein expression block HIV infection are not known. Intriguingly,
94 SUN2 over-expression is associated with alternation of the nuclear envelope shape, suggesting
95 that SUN proteins might interfere with HIV infection through a perturbation of the integrity of
96 the nucleus (Donahue et al., 2016; Lahaye et al., 2016). However, it has not been possible so
97 far to explain how SUN proteins are perturbing cellular and nuclear physiology to impact HIV.
98
99

100 **Results**

101 **SUN1 and SUN2 proteins demonstrate HIV strain-specific antiviral effects**

102 To gain insights in SUN1- and SUN2-mediated antiviral effects on the early steps of HIV
103 infection, we first performed a comparative assessment of the antiviral effect of SUN1 and
104 SUN2 on HIV infection in primary cells. To this end, we over-expressed SUN1 and SUN2 in
105 primary monocyte-derived macrophages (MDMs) using lentiviral vectors (**Figure 1A**). In order
106 to focus on the early phase of infection, cells were infected using single-round HIV-1 and HIV-
107 2 encoding GFP in the place of *Nef*. SUN1 and SUN2 induced an antiviral effect on HIV-1 and
108 HIV-2 (**Figure 1B**). Unexpectedly, HIV-1 was preferentially inhibited by SUN1, while HIV-2
109 was preferentially inhibited in SUN2 (**Figure 1B**). In MDMs, HIV-1 infection is sensitive to
110 Cyclosporin A (CsA). Both SUN1 and SUN2 neutralized the CypA-dependency of HIV-1
111 infection on MDM. We analyzed the progression of HIV-1 and HIV-2 infection in the context
112 of SUN protein expression using RT-qPCR on viral DNA species. For HIV-1, both SUN1 and
113 SUN2 reduced the level of integrated viral DNA (**Figure 1C**). However, SUN1 reduced the
114 total amount of viral DNA, while SUN2 reduced the level of 2-LTR circles. CsA reduced the
115 total amount of viral DNA in control cells and there was no additional reduction following SUN
116 protein expression. For HIV-2, SUN1 and SUN2 significantly reduced 2-LTR circles only.
117 These experiments indicate that SUN1 and SUN2 have strain-specific antiviral effects and that
118 they modify different steps of viral infection.

119 We similarly over-expressed SUN1 and SUN2 in HeLa cells (**Figure 1D**). HIV-1 was
120 preferentially inhibited by SUN1 while HIV-2 was preferentially inhibited by SUN2,
121 recapitulating the situation in MDMs (**Figure 1E, 1F**). In HeLa cells, HIV-1 WT is not sensitive
122 to CsA, but HIV-1 CA N74D is, similar to HIV-1 WT in MDM (De Iaco and Luban, 2014).
123 We thus used this mutant to address the relationship between antiviral effect of SUN and CsA
124 sensitivity. Both SUN1 and SUN2 neutralized CsA sensitivity of HIV-1 CA N74D in HeLa

125 cells (**Figure 1G, 1H**). We next measured the levels of HIV-1 DNA species. SUN1 and SUN2
126 reduced the levels of integrated HIV-1 DNA, and this effect was more pronounced for SUN1
127 (**Figure S1A**). Similar to MDM, SUN1 significantly inhibited the level of total viral DNA while
128 the levels of 2-LTR circles were not significantly reduced. In contrast, SUN2 did not impact
129 the level of total viral DNA, but reduced the level of 2-LTR circles. We thus focused on HeLa
130 cells for additional experiments aiming at characterizing the strain-specific inhibition of SUN1
131 and SUN2.
132
133 **Strain-specific antiviral activity maps to the nucleoplasmic domain of SUN proteins**
134 Cell-cell communication factors of innate immunity, such as interferons and cGAMP, can
135 contribute to antiviral effects on top of cell-intrinsic restriction factors. Using a co-culture of
136 SUN1/2-expressing cells and control cells expressing a fluorescent marker (TagRFP657), we
137 found that the strain-specific effect of SUN1 and SUN2 on HIV-1 and HIV-2 infection is
138 entirely cell-intrinsic in HeLa cells (**Figure 2A**). To determine if SUN1 and SUN2 induced an
139 antiviral state at the cell-intrinsic level through expression of other antiviral genes, we
140 performed a transcriptomic analysis of SUN1 and SUN2 over-expressing cells. Strikingly, we
141 could not detect any differentially expressed gene in this dataset, aside from SUN1 and SUN2
142 themselves (**Figure S1B**). Next, we generated chimeras between SUN1 and SUN2 to map the
143 strain-specific antiviral effect (**Figure 2B, 2C**). We found that the N-terminal nucleoplasmic
144 domains of SUN1 and SUN2 confer strain-specificity (**Figure 2D, 2E**). These results establish
145 that SUN1 and SUN2 exert a cell-intrinsic HIV-strain specific antiviral effect on HIV infection,
146 that maps to the nucleoplasmic domain of SUN proteins.
147
148 **Antiviral effect of SUN proteins at the nuclear envelope**

149 We next sought to study how SUN1 and SUN2 impact cells to inhibit HIV infection. Electron
150 microscopy analysis revealed that both SUN1 and SUN2 over-expression induced deep
151 invaginations of the nuclear envelope, that were more pronounced with SUN2 (**Figure 3A**).
152 This raised the possibility that alteration of the shape of the nucleus could be responsible for
153 the antiviral effect. To test this, we asked if the antiviral effect of SUN occurs at nuclear
154 envelope, or whether it is the results of cytosolic accumulation of SUN proteins. SUN proteins
155 anchor the nucleus in cells by interaction with the KASH domain of cytosolic Nesprin proteins
156 within the perinuclear space. Expression of the isolated KASH domain (SR-KASH) functions
157 as a dominant negative by disrupting the SUN-Nesprin interaction and displacing Nesprins
158 from the nuclear envelope (Starr et al., 2003). We co-expressed SR-KASH with SUN proteins
159 (**Figure 3B**). We found that co-expression of spectrin repeat-KASH (SR-KASH) construct
160 partially rescued the antiviral effect on SUN1 and SUN2 on HIV-1 infection (**Figure 3C**).
161 These results support the notion that SUN proteins have an antiviral activity at the nuclear
162 envelope.
163
164 **Interplay between SUN proteins, HIV infection and the DNA damage response**
165 As a next step, we attempted to characterize the cellular processes affected by elevated SUN
166 proteins. SUN1 and SUN2 are required to limit the accumulation of DNA damage in cells (Lei
167 et al., 2012). Since HIV infection is a DNA-damaging event, we considered the possible
168 interplay between SUN proteins, HIV infection and the DNA damage response. We examined
169 the level of γH2AX, an early marker of the DNA damage response. At baseline, we did not
170 detect modification of γH2AX levels upon SUN1 or SUN2 expression (**Figure 4A, 4B**). To
171 induce DNA damage, we selected etoposide, a topo-isomerase II inhibitor. Interestingly, SUN1,
172 but not SUN2, significantly limited the levels of induced γH2AX after etoposide treatment
173 (**Figure 4A, 4B**). To explore the potential link between DNA damage and infection, we infected

174 HeLa cells in the presence of etoposide for the first 4 hours of the experiment. However,
175 etoposide gradually induces apoptosis of treated cells, as part of its chemotherapeutic effect
176 (Rello-Varona et al., 2006), which hampered our ability to detect viable cells to measure
177 infection after 48 hours. To circumvent this caveat, we cultured cells in the presence of the
178 caspase inhibitor Q-VD-Oph. Q-VD-Oph did not prevent γH2AX induction by etoposide
179 treatment (**Figure 4C**). Etoposide treatment increased HIV-1 infection by 2-fold on average
180 (**Figure 4D**). HIV-2 infection was also increased but significantly at only one dose of etoposide
181 tested, and with a smaller fold change. Next, we combined SUN expression with etoposide to
182 determine the epistatic relationship between DNA damage induction and SUN expression on
183 the level of HIV infection. Here, we used a higher MOI to observe the antiviral effect of SUN
184 proteins. The increased induced by etoposide treatment on control cells was consistently
185 observed across experiments. Interestingly, SUN1 abrogated the proviral effect of etoposide
186 treatment, and in sharp contrast, etoposide treatment rescued cells from the antiviral effect of
187 SUN2 (**Figure 4E, 4F**). Thus, SUN1, which restricts HIV-1 more than SUN2, operates
188 downstream of DNA damage induction, while SUN2 impacts infection upstream of DNA
189 damage.
190

191 **DNA damage induction by ATR inhibition and role of HIV-1 Vpr**

192 Next, we look for a different approach to induce DNA damage that would be functionally linked
193 to the nuclear envelope. ATR is a DNA damage sensor and functions as a checkpoint at the
194 nuclear envelope in response to mechanical stress (Kumar et al., 2014). ATR inhibition
195 heightens DNA damage in cells (Foote et al., 2018). Furthermore, in HIV-1, expression of the
196 accessory protein Vpr causes DNA damage and activates ATR (Roshal et al., 2003), although
197 the relevance of this effect in the context of virion-packaged Vpr is unknown. Considering the
198 significance of ATR at the nuclear envelope and its relationship with Vpr, we asked if DNA

199 damage induction by ATR inhibition, SUN and Vpr are functionally related. We inhibited ATR
200 using AZD6738, a next-generation inhibitor with improved specificity (Foote et al., 2018). As
201 expected, ATR inhibition increased the levels of γH2AX in HeLa cells (**Figure 5A**). We next
202 infected HeLa cells with p24-normalized and sucrose-cushion purified stocks of the HIV-1
203 single-round virus and its HIV-1 vpr-deficient (vpr-) counterpart. ATR inhibition increased
204 HIV-1 infection in HeLa cells by 2-fold, similar to etoposide treatment (**Figure 5B, left panel**).
205 Concomitant SUN protein over-expression inhibited HIV-1 infection, and abrogated the
206 proviral effect of ATR inhibition, again similar to the etoposide treatment. Unexpectedly, the
207 titer of the p24-normalized HIV-1 vpr- was slightly higher than the HIV-1 wild-type counterpart
208 in HeLa cells, and HIV-1 vpr- was insensitive to ATRi (**Figure 5B, right panel**). However,
209 HIV-1 vpr- remained fully sensitive to the antiviral effect of SUN protein expression. In sum,
210 this data supports the idea that increased DNA damage favors HIV-1 infection of HeLa cells,
211 and that SUN1 operates downstream of this to block infection. Intriguingly, this data also
212 revealed that sensitivity to ATR inhibition is a HIV-1 vpr phenotype in single-round infection
213 of HeLa cells.
214
215 **Endogenous Lamin A/C limits HIV-1 infection in HeLa cells**
216 We sought to further explore the relationship between infection, DNA damage and structure of
217 the nuclear envelope. We searched for an orthogonal approach to perturb the nuclear envelope
218 structure and the DNA damage response. Lamin A/C expression is required to maintain a
219 regular nuclear shape (Lammerding et al., 2004) and to protect from DNA damage (Singh et
220 al., 2013). We knocked-down expression of Lamin A/C side-by-side with SUN protein over-
221 expression (**Figure 6A**). Both compromised the regularity of the nuclear envelope shape
222 (**Figure 6B**). To quantify this effect, we measured solidity index as a shape descriptor of the
223 nucleus: solidity values close to 1 indicate smoothly convex nuclei while lower values

224 correspond to deformed, lobulated nuclei, presenting concave invaginations. SUN proteins and
225 Lamin A/C knock-down all increased nuclear envelope deformation, and this effect was less
226 pronounced for SUN1 (**Figure 6C**). The levels of endogenous SUN and Lamin A/C proteins
227 were not reciprocally affected, confirming an independent alteration of the nuclear regularity
228 (**Figure 6A**). After infection, Lamin A/C knock-down unexpectedly increased HIV-1 infection
229 levels by 1.6-fold, while HIV-2 infection was not affected (**Figure 6D**). This shows that
230 endogenous Lamin A/C limits HIV-1 infection in HeLa cells. However, the increase in nuclear
231 envelope shape irregularities does not explain the effects of Lamin A/C depletion and SUN
232 protein expression on HIV infection. Given this opposite effect of SUN expression and Lamin
233 A/C knock-down on HIV-1 infection, we examined if the antiviral effect of SUN proteins
234 requires endogenous lamins. We knocked-down Lamin A/C, Lamin B1 and Lamin B2 and co-
235 expressed SUN proteins (**Figure 6E**). Viable Lamin B1-depleted HeLa cells could not be
236 maintained in culture. Lamin A/C depletion enhanced HIV-1 infection as above, and Lamin B2
237 depletion had no effect (**Figure 6F**). SUN proteins maintained their antiviral effect irrespective
238 of the level of the Lamin A/C and Lamin B2. This shows that the effect of elevated levels of
239 SUN proteins is dominant on the effect of Lamin A/C depletion on HIV-1 infection.
240 Next, we examined the level of γH2AX after etoposide treatment and Lamin A/C depletion.
241 Treatment with a high dose of etoposide (500 μM) for 24 hours induced an increase of γH2AX
242 level in wild-type HeLa cells, while a lower dose (50 μM) had no impact at this time point
243 (**Figure 6G**). In the absence of Lamin A/C, HeLa cells became hyper-sensitive to etoposide
244 treatment (**Figure 6G**). Thus, the increase in HIV-1 infection observed after Lamin A/C
245 depletion correlates with an increased sensitivity to DNA damage. Altogether, these results
246 establish a functional correlation between the effect of SUN protein and endogenous Lamin
247 A/C on HIV-1 infection and on the cellular response to DNA damage induced by an exogenous
248 compound.

249

250 **Elevated SUN proteins do not alter NPC density, passive import or cell stiffness**

251 We next sought to identify the endogenous mechanisms that delineate the effects of elevated
252 SUN proteins and endogenous Lamin A/C depletion on infection. We characterized biophysical
253 and structural parameters in SUN-expressing cells. HIV-1 enters the nucleus through the NPC.
254 We identified NPC using Nup153 on tangential confocal sections of the nuclear envelope by
255 microscopy (**Figure S2A**). Over-expression of SUN proteins did not alter the density of the
256 NPC at the nuclear envelope (**Figure S2B**). To determine if the NPC functionality was impaired
257 by SUN protein over-expression, we measured passive diffusion through the NPC using a
258 Fluorescence Recovery After Photobleaching (FRAP) assay on ubiquitous GFP. SUN proteins
259 had no impact on the rate of recovery of nuclear GFP (**Figure S2C, Movie 1**). Lamin A/C
260 depletion reduces stiffness of the nuclear, resulting in a floppy nucleus (Lammerding et al.,
261 2004). To determine if SUN proteins expression induced the opposite to match the effects on
262 infection, we measured stiffness using a microfabricated device that pushes cells through a
263 constricted space by applying a fixed liquid pressure. While we confirmed that Lamin A/C
264 depleted cells have reduced stiffness, expression of SUN proteins had no impact on this
265 parameter (**Figure S2D**).

266

267 **HIV-1 infection requires movement of the chromatin**

268 Next, we turned our attention to the endogenous state of chromatin. We performed live-imaging
269 of cells with a DNA stain after SUN expression or Lamin A/C depletion. We visually noticed
270 that the behavior of the nuclei was different between conditions: SUN1 and SUN2 appeared to
271 lock the nucleus in place, while nuclei of Lamin A/C-depleted cells appeared highly dynamic
272 (**Figure 7A, Movies 2–6**). We first asked whether the extent of chromatin movement inside the
273 nuclei was altered. We isolated movies of single nuclei and performed a registration step to

274 normalize X-Y positions and angle, therefore suppressing general nuclei displacement and
275 rotation. We next measured chromatin movement in the registered nuclei by performing a
276 particle image velocimetry (PIV) analysis. Strikingly, SUN1 and SUN2 over-expression
277 reduced the displacement of chromatin over time, and this effect was more pronounced with
278 SUN1, while Lamin A/C depletion had the converse effect (**Figure 7B, S3A**). HeLa cells also
279 exhibited seemingly random rotation of their nuclei, at various speeds and frequencies. Using
280 the same dataset, we measured the rotation of the whole nucleus relative to the cytoplasm. We
281 corrected the translational displacement of nuclei by registration and measured the angle of
282 rotation over time using a custom-made analysis script (**Movie 7**). SUN1 and SUN2 reduced
283 the average speed of nuclear rotation and the fraction of time spent rotating above a threshold
284 of 1° (**Figure 7C, S3B**). The rotation of Lamin A/C-depleted nuclei was visibly higher than
285 controls, but could not be reliably quantified due to the high levels of chromatin displacement
286 that hampered the ability to set reference points. Overall, these results indicate that the impact
287 of SUN and Lamin A/C proteins on HIV-1 infection is associated with the movement of
288 chromatin within the cells.
289
290

291 **Discussion**

292 Our findings reveal that SUN1 and SUN2, though paralogs, have distinct effects on HIV
293 infection. SUN1 overexpression is more efficient at inhibiting HIV-1 than SUN2. Meanwhile,
294 SUN2 shows a preferential antiviral activity against HIV-2. An analysis of the viral step being
295 impacted by the two proteins also reveals a discrepancy between the two: while both SUN1 and
296 SUN2 over-expression reduces the level of integrated HIV-1 DNA, SUN1 also inhibits total
297 viral DNA amount while SUN2 reduces the levels of 2-LTR circles, a hallmark of nuclear entry.
298 We also reveal that SUN1 and SUN2 differ in their response to DNA damage and its impact on
299 HIV infection. SUN1 limits the response to etoposide as measured by the levels γH2AX, while
300 SUN2 enhances it. Strikingly, etoposide largely rescues the antiviral effect of SUN2 over-
301 expression on HIV-1, while SUN1 is resistant to this effect. This result suggests that SUN1 and
302 SUN2 may differ in the ways in which they establish interactions and functions within the
303 nucleus, in line with previously reports showing non-redundant effects of SUN1 and SUN2 (Lei
304 et al., 2009; Liu et al., 2007).

305 Etoposide treatment also enhances the infection by HIV-1 by two-fold in HeLa cells in the
306 absence of SUN protein over-expression, while HIV-2 is largely unaffected. Such proviral
307 effect of DNA damage has been previously observed in conditions of integrase inhibition
308 (Ebina et al., 2012; Koyama et al., 2013). In contrast, it was previously reported that etoposide
309 treatment inhibits HIV-1 infection in monocyte-derived macrophages (Mlcochova et al., 2018).
310 We speculate that this is explained by the presence of a SAMHD1-dependent block in this cell
311 type induced by etoposide in macrophages, but not in HeLa cells.

312 Similar to etoposide, ATR inhibition also enhances HIV-1 infection by 2-fold. The lack of
313 requirement for ATR in HIV infection is consistent with prior studies (Ariumi et al., 2005;
314 DeHart et al., 2005). Interestingly, the effect of ATR inhibition requires the presence of the Vpr
315 gene in HIV-1. As a virus-encoded gene, Vpr has be shown to induce an ATR-dependent G2

316 arrest of the cell cycle (Zimmerman et al., 2006). Using purified and p24-normalized virus
317 preparations, we made the unexpected observation that the Vpr-deficient virus is actually as
318 infectious as the wild-type virus stimulated with ATR inhibition. In other words, in this
319 asynchronous system of single-round infection of HeLa cells, the presence of the Vpr gene
320 appears to provide a counter-intuitive two-fold reduction in infectivity of the virus, which is
321 alleviated by ATR inhibition. However, Vpr has been associated with an enhanced expression
322 for the viral LTR during G2 arrest (Goh et al., 1998). We speculate that in terms of viral
323 replicative fitness, the reduction in single-round infectivity entailed by Vpr is cancelled out by
324 this proviral effect of Vpr during G2 arrest. Of note, both SUN1 and SUN2 over-expression
325 inhibit HIV-1 infection irrespective of ATR inhibition. In contrast, etoposide rescues the
326 antiviral effect of SUN2 on HIV-1, raising the possibility that ATR itself might play a role in
327 the rescue of the SUN2 antiviral effect.
328 Multiple lines of evidence from our work indicate that the structure of the nuclear envelope
329 impacts HIV infection. The ability of SR-KASH to partially rescue the antiviral effects of SUN
330 proteins indicates that the LINC complex, which is located at the nuclear envelope, is involved.
331 Despite the important morphological changes induced by SUN protein expression, we did not
332 observe any change at the level of gene expression, suggesting that any SUN-mediated effect
333 on the nucleus and, subsequently, on HIV infection is post-transcriptional. ATR is enriched at
334 the nuclear envelope during S phase and upon mechanical stretching, two processes that
335 increase nuclear envelope stress (Kumar et al., 2014). ATR-deficient cells exhibit deformed
336 nuclei, reminiscent of Lamin A/C depletion or SUN protein overexpression (Kidiyoor et al.,
337 2020). Vpr over-expression was previously shown to induce herniations of the nuclear envelope
338 associated with defects in the nuclear lamina (de Noronha et al., 2001). We also find that
339 endogenous Lamin A/C has an antiviral effect, in agreement with a previous study (Sun et al.,
340 2018).

341 We examined several effects of SUN protein over-expression and endogenous Lamin A/C on
342 nuclear shape, stiffness, NPC distribution and function, and chromatin dynamics. The effects
343 on HIV-1 infection match the effects of the proteins on chromatin dynamics: decreased HIV-1
344 infection is associated with a decreased chromatin motility inside the nucleus, and decreased
345 rotation of the nucleus relative to the cytoplasm. In contrast, HIV-2 infection is more
346 susceptible to SUN2 than SUN1, and it is not affected by Lamin A/C depletion. Overexpresion
347 of SUN2 deforms nuclei more than SUN1 but internal chromatin dynamics and nuclear rotation
348 are less impacted. This strain specificity could be linked to a different dependency on host
349 factors between HIV-1 and HIV-2 (Braaten and Luban, 2001). SUN and Lamin proteins have
350 been previously linked to chromatin mobility and nuclear rotation (Ji et al., 2007; Lottersberger
351 et al., 2015; Oza et al., 2009; Ranade et al., 2019). Interestingly, nuclear rotation is required for
352 optimal infection by another nuclear-invading virus, HCMV (Procter et al., 2018). This rotation
353 is required to promote spatial chromatin segregation that favors viral gene expression (Procter
354 et al., 2018). We propose that HIV-1 infection requires nuclear rotation and chromatin
355 movements for optimal integration and subsequent viral expression.
356 Our results highlight the interplay between HIV infection, structural proteins of the nuclear
357 envelope and the DNA damage response. Nuclear rotation and chromatin dynamics emerge as
358 potentially important factors that control HIV infection. Future studies will be required to
359 address the underlying molecular mechanisms, which we anticipate will require the use of
360 biophysical approaches. It will also be important to examine these mechanisms in the frame of
361 the diversity of lentiviruses, and its relevance for viral replication and innate immune sensing
362 mechanisms in primary target cells.
363

Acknowledgments

We thank N. De Silva for setting up the γH2AX intranuclear staining; V. Teixeira Rodrigues for assistance with primary macrophages; P. Benaroch for critically reading this manuscript; M. Piel, N. De Silva, N. Jeremiah and A. Williart for discussions. We acknowledge the imaging facility (PICT-IBiSA, LABEX ANR-10-LBX-0038, ANR-10-IDEX-0001-02 PSL, France-BioImaging, ANR-10-INSB-04), and Audrey Rapinat and David Gentien from the Genomics Platform at Institut Curie. This work was supported by Institut Curie, INSERM, and by grants from the Agence Nationale de la Recherche (ANR-10-IDEX-0001-02 PSL, ANR-11-LABX-0043, ANR-17-CE15-0025-01, ANR-19-CE15-0018-01, ANR-18-CE92-0022-01), the Agence Nationale de la Recherche sur le SIDA (ECTZ36691, ECTZ25472, ECTZ71745), Sidaction (VIH2016126002, 17-1-AAE-11097-2). AB was supported by fellowships from PSL University and Fondation pour la Recherche Médicale.

379 **Figure Legends**

380

381 **Figure 1 Distinct antiviral activities of SUN1 and SUN2 against HIV-1 and HIV-2**

382 **(A)** Detection of SUN1, SUN2 and actin in MDMs transduced with mTagBFP-2A control,
383 SUN1 or SUN2 lentivectors (representative of n = 3).

384 **(B)** Left, viral titers as infectious units (i.u.) per mL based on percentages of GFP^+ MDMs 48
385 hours after infection with serial dilutions of HIV-1 or HIV-2 encoding GFP in Nef and
386 pseudotyped with VSV-G, with or without 2 μM CsA (n = 9 donors, paired RM ANOVA one-
387 way on Log-transformed titers with Sidak post-test, line at mean). Right, ratios of titer fold
388 changes (FC) control over SUN1 (SUN1 FC) or control over SUN2 (SUN2 FC).

389 **(C)** Detection of HIV-1 total DNA, 2-LTR circles DNA and integrated DNA by RT-qPCR at
390 24 hours after infection with HIV-1 or HIV-2 (dilution factor: 0.17) of MDMs transduced with
391 mTagBFP-2A control, SUN1 or SUN2 lentivectors. Reverse transcriptase inhibitors
392 Azidothymidine (AZT; 24 μM) and Nevirapine (NVP; 10 μM) were added during infection
393 when indicated (n=4 donors, paired RM ANOVA one-way with Sidak post-test, line at mean ±
394 SEM).

395 **(D)** Detection of SUN1, SUN2 and actin in HeLa cells transduced with mTagBFP-2A control,
396 SUN1 or SUN2 lentivectors.

397 **(E)** GFP expression in BFP-positive HeLa cells transduced with mTagBFP-2A control, SUN1
398 or SUN2 lentivectors, 48 hours after infection with indicated dilutions of HIV-1 and HIV-2
399 (representative data from one experiment at the indicated dose of virus).

400 **(F)** Left, Viral titers based on percentages of GFP^+ cells after infection with serial dilutions of
401 virus as in **(E)** (n = 6, paired RM ANOVA one-way on Log-transformed titers, with Dunnet's
402 post-test, line at mean). Right, ratios calculated as in **(B)**.

403 **(G)** Percentage of GFP^+ in BFP^+ HeLa cells transduced with mTagBFP-2A control, SUN1 or
404 SUN2 lentivectors, 48 hours after infection with serial dilutions of HIV-1 or HIV-1 CA N74D,
405 with or without treatment with 2 µM of CsA (n = 3 independent experiments).
406 **(H)** Viral titers as in (G) (n = 3, paired RM ANOVA one-way on Log-transformed titers with
407 Sidak's post-test, line at mean).
408 Ctrl = control, $^{*}p < 0.05$, $^{***}p < 0.001$, $^{****}p < 0.0001$; ns, not statistically significant.
409
410 **Figure 2 Mapping of the strain-specific antiviral activity of SUN proteins**
411 **(A)** mTagBFP-2A Ctrl, mTagBFP-2A-SUN1 and mTagBFP-2A-SUN2 expressing HeLa cells
412 were co-cultured at a 1:1 ratio with HeLa cells expressing TagRFP657-2A and infected with
413 serial dilutions of HIV-1 and HIV-2. Titers were calculated based on percentage of GFP^+ cells
414 48 hours post-infection dilutions within the indicated populations (n=3 independent
415 experiments, paired RM ANOVA one-way on Log-transformed titers with Sidak's post-test,
416 line at mean).
417 **(B)** Schematic representation of chimeric proteins between full-length SUN1 (red) and SUN2
418 (blue). Amino-acid residues retained in hybrid proteins are indicated within brackets.
419 **(C)** Detection of SUN1, SUN2 and actin in HeLa cells transduced with the indicated mTagBFP-
420 2A lentivectors. Two antibodies targeting SUN2 that recognize different epitopes within the
421 protein were used.
422 **(D)** Percentage of GFP^+ in BFP^+ HeLa cells transduced with the indicated mTagBFP-2A
423 lentivectors, 48 hours after infection with serial dilutions of HIV-1 or HIV-2 (n=3 independent
424 experiments).
425 **(E)** Viral titers based on percentages of GFP^+ cells shown in **(D)** (n=3, paired RM ANOVA
426 one-way with Sidak's post-test, line at mean).
427 Ctrl = control, $^{*}p < 0.05$, $^{**}p < 0.01$, $^{***}p < 0.001$, $^{****}p < 0.0001$; ns, not statistically significant.

428

429 **Figure 3 SUN proteins inhibit HIV infection at the nuclear envelope**

430 **(A)** Representative electron micrograph showing nuclei in control, SUN1 and SUN2
431 overexpressing HeLa cells (scale: 10, 2 and 5 µm respectively).

432 **(B)** Detection of SUN1, SUN2, GFP and actin in HeLa cells transduced with TagRFP657-
433 expressing control, SUN1 or SUN2 lentivectors, combined with control GFP or SR-KASH DN
434 fused to GFP expressing lentivectors. The same lysates were loaded onto two separate
435 membranes, the housekeeping control is shown for both.

436 **(C)** Top, percentage of BFP^+ within $tagRFP657^+$ HeLa cells 48 hours after infection with serial
437 dilutions of HIV-1 encoding BFP in the place of Nef, pseudotyped with VSV-G. Bottom, viral
438 titers based on percentages of BFP^+ cells (n=3, paired RM ANOVA one-way on Log-
439 transformed titers, with Sidak's post-test, line at mean ± SEM).

440 Ctrl = control, $^*p < 0.05$, $^{**}p < 0.01$, $^{***}p < 0.001$; ns, not statistically significant.

441

442 **Figure 4 Interplay between HIV-1 infection, SUN protein and the DNA damage response**

443 **(A)** Viability and γH2AX intracellular staining in HeLa cells transduced with mTagBFP-2A
444 control, SUN1 or SUN2 lentivector, 24 hours after treatment with 500 µM of etoposide or 1%
445 DMSO as control (representative experiment from n = 3).

446 **(B)** Quantification of $\gamma H2AX^+$ HeLa cells treated as in **(A)** (n=4, paired RM ANOVA one-way
447 with Sidak's post-test, line at mean).

448 **(C)** Quantification of $\gamma H2AX^+$ HeLa cells 24 hours after a 4-hour treatment with 5 µM, 50 µM
449 etoposide or corresponding DMSO control. 50 µM of Q-VD-Oph were present throughout the
450 experiment (n=3, paired RM ANOVA one-way with Sidak's post-test, line at mean ± SEM).

451 **(D)** Top, percentage of GFP^+ HeLa cells 48 hours after infection with two dilutions of HIV-1
452 or HIV-2, treated as in **(C)**. Cells were treated and infected simultaneously, the drugs and the

453 virus were washed out at 4 hours post-treatment/infection. 50 μM of Q-VD-Oph were
454 maintained throughout the experiment. Bottom, viral titers based on percentages of GFP^+ cells
455 (n=3, paired RM ANOVA one-way with Sidak's post-test, line at mean).
456 **(E)** Quantification of $\gamma H2AX^+$ HeLa cells, transduced with mTagBFP-2A control, SUN1 or
457 SUN2 lentivectors, 4 hours after treatment with 50 μM of etoposide or corresponding DMSO
458 control (n=3, paired RM ANOVA one-way with Sidak's post-test, line at mean ± SEM).
459 **(F)** Left, percentage of GFP^+ cells in BFP^+ HeLa cells expressing control, SUN1, SUN2
460 lentivectors and treated as in **(E)**, 48 hours after infection with purified HIV-1 env-nef-,
461 expressing GFP in the place of Nef and pseudotyped with VSV-G. Right, GFP+ percentages at
462 viral dilution 0.02 (n=3, experimental pairs are indicated; RM ANOVA two-way test,
463 uncorrected Fischer' LSD). 50 μM of Q-VD-Oph were maintained throughout the experiment.
464 Ctrl = control, hpt = hours post treatment, $^{*}p < 0.05$, $^{**}p < 0.01$, $^{***}p < 0.001$, $^{****}p < 0.0001$; ns,
465 not statistically significant.
466
467 **Figure 5 DNA damage induction by ATR inhibition stimulates HIV-1 infection in a Vpr-**
468 **dependent manner**
469 **(A)** Top, γH2AX intracellular staining in mTagBFP-2A control HeLa cell line, 24 hours after
470 treatment with either 1 μM of AZD6738 or 0.01% DMSO (representative experiment). Bottom,
471 quantification of specific γH2AX staining as geometric mean fluorescence intensity (GeoMFI)
472 of the antibody signal divided by the GeoMFI of the isotype control (n=4, paired t-test, $^{*}p <$
473 0.05, line at mean ± SEM).
474 **(B)** Viral titers based on percentages of GFP^+ cells, within BFP^+ HeLa cells expressing Ctrl,
475 SUN1 or SUN2 lentivector, with or without treatment with 1 μM of AZ6738, 48 hours after
476 infection with serial dilutions of purified, p24-normalized, HIV-1 env-nef- or HIV-1 env-nef-

477 vpr- encoding GFP in the place of Nef, pseudotyped with VSV-G (n=3, paired RM ANOVA
478 one-way with Sidak's post-test, line at mean ± SEM).
479 Ctrl = control, hpt = hours post treatment, $^{*}p < 0.05$, $^{***}p < 0.001$, ns, not statistically significant.
480
481 **Figure 6 Interplay between HIV-1 infection, Lamin A/C protein and the DNA damage**
482 **response**
483 **(A)** Detection of SUN1, SUN2, Lamin A/C and actin in HeLa cells transduced with mTagBFP-
484 2A control, SUN1 or SUN2 lentivectors, negative control LacZ (shLACZ) or lamin A/C
485 (shLMNA) targeting shRNA-encoding lentivectors.
486 **(B)** Nuclei of HeLa cells lines as in (A) visualized on fixed cells using SiR-DNA dye. Images
487 show signal from an individual, central confocal plane, scale bar is at 10 µm.
488 **(C)** Solidity index of nuclei as in **(B)**. Legend indicates total number of nuclei analyzed per cell
489 line (representative of n=2 experiments, one on fixed cells and one with live imaging). Unpaired
490 ANOVA one-way with Sidak's, line at median.
491 **(D)** Viral titers based on percentages of GFP^{+} HeLa cells lines from **(A)** after infection with
492 serial dilutions of HIV-1 and HIV-2 (n=3, paired RM ANOVA one-way with Sidak's post-test,
493 line at mean).
494 **(E)** Detection of SUN1, SUN2, Lamin A/C, Lamin B2 and actin in HeLa cells co-transduced
495 with mTagBFP-2A control, SUN1 or SUN2 lentivectors and with LacZ, lamin A/C or lamin
496 B2 (shLMNB2) targeting shRNA-encoding lentivectors.
497 **(F)** Viral titers based on percentages of GFP^{+} HeLa cells as shown in **(E)** after infection with
498 serial dilutions of HIV-1 and HIV-2 (n=3, paired RM ANOVA one-way with Sidak's post-test,
499 line at mean).

500 **(G)** Quantification of γH2AX^{+} HeLa cells transduced with either a LacZ or lamin A/C targeting
501 shRNA lentivector, 24 hours after treatment with indicated doses of etoposide or DMSO control
502 (n=3, line at mean ± SEM).
503 Ctrl = control, hpt = hours post treatment, $^{*}p < 0.05$, $^{**}p < 0.001$, $^{***}p < 0.001$, $^{****}p < 0.0001$;
504 ns, not statistically significant.
505
506 **Figure 7 SUN protein overexpression and endogenous Lamin A/C limit movements of the**
507 **chromatin**
508 **(A)** Particle Image Velocimetry (PIV)-of DNA within nuclei of HeLa cells transduced with
509 mTagBFP-2A control, SUN1 or SUN2 lentivectors, negative control LacZ or lamin A/C
510 targeting shRNA-encoding lentivectors. PIV is shown for individual representative nuclei of
511 each cell line, top panels show overall flow and bottom panels show individual vectorial
512 displacements between two consecutive frames corresponding to two minutes of imaging. Scale
513 bar corresponds to 5 µm. Reference color scale for pixel displacement per time frame is shown
514 on left.
515 **(B)** Quantification of DNA displacement as µm/min from images as in **(A)**. Results are shown
516 for one experiment from n = 2. Left, unpaired ANOVA one-way with Sidak's post-test, line at
517 mean. Right, unpaired student t-test, line at mean.
518 **(C)** Quantification of nuclear rotation speed as degrees/minute (top) and rotation duration as
519 fraction of total time spent rotating over a threshold of 1° (bottom) in HeLa cells transduced
520 with mTagBFP-2A control, SUN1 or SUN2 lentivectors and imaged as in **(A)**. Results are
521 shown for one experiment from n = 2. Unpaired ANOVA one-way with Sidak's (top) or
522 Turkey's (bottom) post-test, line at mean.
523 Ctrl = control, $^{*}p < 0.05$, $^{**}p < 0.01$, $^{****}p < 0.0001$; ns, not statistically significant.
524

525 **Supplemental Material**

526 **Figure S1 HIV-1 DNA quantification and gene expression analysis of SUN-overexpressing**
527 **cells**

528 **(A)** Detection of HIV-1 total DNA, 2-LTR circles DNA and integrated DNA by RT-qPCR at
529 24 hours after infection (dilution factor: 0.1) of HeLa cells transduced with mTagBFP-2A
530 control, SUN1 or SUN2 lentivectors. AZT (24 μM) was added during infection when indicated
531 (n=3, paired RM ANOVA one-way with Turkey's post-test, line at mean ± SEM).

532 **(B)** Differential gene expression in SUN1 (Left) and SUN2 (Right) overexpressing cells over
533 control cells (FC, fold change; FDR, false discovery rate). Over-expressed SUN2 was codon-
534 optimized, rendering it sub-optimal for probe-based detection.

535 Ctrl = control, $^{*}p < 0.05$, $^{**}p < 0.001$, $^{***}p < 0.001$; ns, not statistically significant.

536

537 **Figure S2 Analysis of NPC density, passive nuclear import and cellular stiffness of SUN-**
538 **overexpressing cells**

539 **(A)** Left, confocal imaging of NUP153 staining in HeLa cells. Right, blow-up or region of
540 interest and detection of individual of NPC (red) using "Find Maxima" function. A
541 representative nucleus of cells overexpressing mTagBFP-2A-SUN2 is shown.

542 **(B)** Quantification of NPC density per μm^2 in nuclei from HeLa cells transduced with
543 mTagBFP-2A control, SUN1 or SUN2 lentivectors, imaged and analyzed as in **(A)** (total
544 number of nuclei analyzed per cell line are indicted, n=1 experiment; un-paired ANOVA one-
545 way with Sidak's post-test, line at mean).

546 **(C)** Passive diffusion from the cytoplasm to the nucleus measured by FRAP, in HeLa cells
547 transduced with mTagBFP-2A control, SUN1 or SUN2 lentivectors and a lentivector encoding
548 GFP. Top, representative layout of a photobleached control HeLa cell: imaging starts at t = 0
549 after high intensity laser exposure and ends at t = 80 seconds, when fluorescence in the nucleus

550 has been recovered (scale bar: 5 µm). Bottom left: GFP intensity recovery over time (s). For
551 each individual cell, the background intensity was subtracted and intensity was normalized to
552 0 at t0 after photobleaching while the max intensity reached during the course of each
553 measurement was set to 1. Curves show mean and standard deviation per time point across
554 indicated number of cells per condition. Bottom right, hillslopes for each cell were calculated
555 via non-linear regression fit (total number of nuclei analyzed per cell line are indicated, n=1
556 experiment; un-paired ANOVA one-way with Dunnett's post-test, line at mean ± SEM).
557 **(D)** Measurement of nuclear rigidity. Left, representative image showing tagBFP-2A-Ctrl HeLa
558 cells stained with SiR-DNA and going through microchannels under externally-applied
559 pressure. The green arrow indicates the elongation of SiR-DNA staining within the channel,
560 which is measured over time as a readout for nuclear rigidity. Right, quantification of nuclear
561 rigidity across HeLa cell lines described in **(6A)** over time (the number of nuclei measured per
562 cell line is indicated within brackets, n = 3 independent experiments).
563 Ctrl = control, ns, not statistically significant.
564
565 **Figure S3 SUN protein over-expression and endogenous Lamin A/C limit movements of**
566 **the chromatin, second experiment.**
567 **(A)** Quantification of DNA displacement as µm/min from images as in Figure 7B, second
568 experiment. Top, unpaired ANOVA one-way with Sidak's post-test, line at mean. Bottom,
569 unpaired student t-test, line at mean.
570 **(B)** Quantification of nuclear rotation speed as degrees/minute (top) and rotation duration as
571 fraction of total time (bottom) spent rotating over a threshold of 1°, as in Figure 7C, second
572 experiment. Unpaired ANOVA one-way with Sidak's (top) or Turkey's (bottom) post-test, line
573 at mean.
574 Ctrl = control, $^{*}p < 0.05$, $^{*}p < 0.01$ $^{***}p < 0.001$, $^{****}p < 0.0001$; ns, not statistically significant.

575

576

577 **Movie 1 Passive diffusion from the cytoplasm to the nucleus measured by FRAP.**

578 Representative movie of a HeLa cell overexpressing mTagBFP-2A-Ctrl and ubiquitous GFP
579 lentivectors. Immediately prior to imaging, high intensity 488 nm laser was directed to a small
580 region within the nucleus to bleach the GFP signal within this compartment. Imaging of the
581 whole cell starts at t = 0 immediately after bleaching. Recovery of the GFP signal in the nucleus
582 is observed as GFP diffuses back in from the cytoplasm until equilibrium is obtained. One frame
583 was taken every 2 seconds.

584

585 **Movies 2 Quantification of chromatin dynamics in mTagBFP-2A-overexpressing control**
586 **HeLa cells.**

587 Chromatin dynamics assessed by PIV. The analysis was performed on live confocal imaging
588 of DNA staining using SiR-DNA. An image was taken every 2 minutes. The left panel shows
589 registration of the object (one nucleus) across 10 time frames while the right panel shows the
590 flow of pixel clusters (interrogation windows) within the object, across consecutive time
591 frames. Warmer colors indicate high levels of displacement while cold colors indicate more
592 static regions. Scale bar corresponds to 5 µm.

593

594 **Movie 3 Quantification of chromatin dynamics in mTagBFP-2A-SUN1-overexpressing**
595 **HeLa cells.**

596 Analysis was performed as for Movie 2.

597

598 **Movie 4 Quantification of chromatin dynamics in mTagBFP-2A-SUN2-overexpressing**
599 **HeLa cells.**

600 Analysis was performed as for Movie 2.

601

602

603 **Movie 5 Quantification of chromatin dynamics in HeLa cells expressing a control shRNA**

604 **against LacZ.**

605 Analysis was performed as for Movie 2.

606

607 **Movie 6 Quantification of chromatin dynamics in HeLa cells expressing a shRNA against**

608 **Lamin A/C.**

609 Analysis was performed as for Movie 2.

610

611 **Movie 7 Measurement of nuclear rotation in a HeLa cell.**

612 The analysis was performed on live confocal imaging of DNA staining using SiR-DNA. An

613 image was taken every 2 minutes, for a total duration of 60 minutes. The angle was measured

614 in reference to an image containing 2 fixed points (one at the center and one on the edge of the

615 nucleus). In this example, HeLa overexpressing mTagBFP-2A control are shown.

616 **Materials and methods**

617 Constructs

618 The plasmid constructs for lentiviral expression and HIV infection used in this study are listed
619 in **Table 1**. pTRIP-SFFV-tagBFP-2A-SUN1 Dharmacon was generated by overlapping PCR
620 cloning from commercially bought cDNA (MGC cDNA cloneID: 40148817) into pTRIP-
621 SFFV-tagBFP-2A (Cerboni et al., 2017). pTRIP-SFFV-tagBFP-2A-ntSUN2 was generated by
622 overlapping PCR mutagenesis from pLX304-SUN2 (Lahaye et al., 2016) into pTRIP-SFFV-
623 tagBFP-2A with concomitant introduction of silent mutations that are not targeted by SUN2
624 shRNA 4 and 5 (respectively GCCTATTCAGACGTTTCACTTT to
625 ACCGATCCAAACTTTCCATTTC and GAGGAAATCCAGCAACATGAAG to
626 ACGCAAGAGTTCTAATATGAAA). pTRIP-SFFV-tagBFP-2A-SUN1 Dharmacon (1-298)-
627 ntSUN2 (220-717) and pTRIP-SFFV-tagBFP-2A-ntSUN2 (1-219)-SUN1 Dharmacon (299-
628 785) were generated by overlapping PCR cloning from the full-length constructs. pTRIP-
629 SFFV-tagRFP657-2A-SUN1 and pTRIP-SFFV-tagRFP657-2A-ntSUN2 were generated via
630 restriction enzyme digestion from the tagBFP expressing vectors and ligation into pTRIP-
631 SFFV-TagRFP657-2A backbone. HIV-GFP env-nef- was generated by PCR-mediated
632 insertion of the Vpr+Vif+Vpu+ cassette from NL4-3 into HIV-GFP (Manel et al., 2010). HIV-
633 GFP env-nef-vpr- was generated by overlapping PCR mutagenesis from HIV-GFP env-nef-,
634 introducing a frameshift mutation within *vpr,* after the codon corresponding to amino-acid I63
635 (gaattc to gaaTTAAttc). HIV-mTagBFP2 and HIV-2 ROD9 ΔenvΔnef mTagBFP2+ were
636 obtained via overlapping PCR mutagenesis, replacing GFP with the mTagBFP from pTRIP-
637 SFFV-mTagBFP-2A.

638

639 Cells

640 GHOST (GHOST X4R5), 293FT and HeLa cells were cultured in DMEM with Glutamax, 10%
641 fetal bovine serum (FBS) (Corning), and penicillin-streptomycin (Gibco). Human peripheral
642 blood mononuclear cells (PBMCs) were isolated from buffy coats from normal human donors
643 (approved by the Institut National de la Santé et de la Recherche Médicale ethics committee)
644 using Ficoll-Paque PLUS (GE). $CD14^+$ cells were isolated by a positive selection with anti-
645 human CD14 magnetic beads (Miltenyi) from PBMCs. To obtain macrophages (MDMs),
646 $CD14^+$ cells were cultured in RPMI with Glutamax, 5% FBS (Eurobio), 5% human serum
647 (Sigma), Penicillin-Streptomycin, Gentamicin (50 µg/ml, GIBCO) and HEPES (GIBCO) in the
648 presence of recombinant human M-CSF (Miltenyi) at 50 ng/ml. Fresh media was added at day
649 5 or 6, and cells were treated/infected at day 9, after detachment via incubation with StemPro
650 Accutase Cell Dissociation Reagent (Gibco) for 30 minutes at 37°C. Drug treatments performed
651 on cultured cells are listed in **Table 2**.
652
653 Virus production
654 Viral particles were produced by transfection of 293FT cells in 6-well plates with 3 µg DNA
655 and 8 µl TransIT-293 Transfection Reagent (Mirus Bio) per well. For VSV-G pseudotyped
656 SIVmac virus-like particles (VLPs), 0.4 µg CMV-VSVG and 2.6 µg $pSIV3^+$ was used. For
657 VSV-G pseudotyped HIV-1 and HIV-2 GFP or BFP-reporter viruses, 0.4 µg CMV-VSVG and
658 2.6 µg HIV DNA was used. For over-expression or sh-RNA mediated knock-down, 0.4 µg
659 CMV-VSVG, 1 µg psPAX2 and 1.6 µg of lentivector of interest were combined. One day after
660 transfection, media was removed, cells were washed once, and 3 ml per well of RPMI medium
661 with Glutamax, 10% FBS (Gibco), PenStrep (Gibco), 50µg/ml Gentamicin (Gibco) and 0.01 M
662 HEPES (Gibco) were added. Viral supernatants were harvested 1 day later, filtered using
663 0.45 µm pore filters, used fresh or aliquoted and frozen at −80°C. When required, the virus was
664 purified and concentrated on a 20% sucrose cushion in PBS in Ultra Clear Centrifuge tubes

665 (Beckman Coulter), via ultracentrifugation at 4°C at 31,000 *x g* in a SW32Ti swinging bucket
666 rotor (Beckman Coulter). Viral pellets were then resuspended in complete medium at a 100-
667 fold concentration compared to crude. Viral titers were measured on GHOST cells (titration as
668 previously described (Manel et al., 2010) or using HIV-1 p24 ELISA (XpressBio). ELISA
669 absorbance acquisitions were acquired on a FLUOstar OPTIMA (BMG Labtech) and data were
670 analyzed and exported to Excel with MARS Data Analysis Software (BMG Labtech).
671
672 Cell Transduction for protein overexpression or knockdown
673 HeLa cells were counted and seeded in 6-well plates on the day prior to transduction. Purified
674 virus was added at a 2:1 volume ratio on medium containing protamine at a final concentration
675 of 1 µg/ml. $CD14^+$ monocytes were seeded in 10-cm dishes in the presence of 50 ng/ml M-CSF
676 to induce differentiation into macrophages and transduced with purified SIVmac VLPs and
677 lentiviruses carrying vector of interest, mixed at a 1:1 ratio. Human serum was added at day 1
678 post transduction. Transductions of monocytes was performed in the presence of protamine at
679 a final concentration of 1 µg/ml. HeLa cells were washed once in PBS and passaged at 48 hours
680 post transduction with or without 2 µg/ml of puromycin. For MDMs, medium was replaced at
681 day 5-6 post transduction. Over-expression was assessed by quantification of fluorescent
682 reporter signal via flow cytometry on a BD FACSVerse flow cytometer. Both over-expression
683 and protein knock-down were confirmed by Western Blotting at day of experiment.
684
685 Cell infection
686 HeLa, GHOST and MDMs (day 8-9 post transduction) were seeded and infected in the presence
687 of 1 µg/ml of protamine with serial dilutions of frozen viral stocks in a BSL-3 laboratory. Virus
688 was removed at 48 hours post-infection, cells were washed, harvested, stained for viability
689 using Fixable Viability Dye eFluor 780 in PBS where required, fixed in 1% paraformaldehyde

690 (PFA; Electron Microscopy Sciences) and analyzed for GFP or BFP positivity via flow
691 cytometry on a BD FACSVerse flow cytometer. Viral titers were calculated based on seeded
692 cell number and the percentages of infected cells, within the linear range of infection.
693
694 HIV DNA quantification
695 HeLa cells and MDMs were infected as described, with the addition of infected wells treated
696 with RT inhibitors as negative control. For this purpose, either 24 μM of AZT (Sigma) or 10
697 μM of NVP (Sigma) were used. After 24 hours, cells were washed in PBS and harvested. Total
698 DNA was extracted from cell pellets using NucleoSpin Tissue (Macherey-Nagel) kit, as per
699 manufacturer's protocol. Real-time PCR analysis was performed as previously described
700 (Lahaye et al., 2013). Each sample was measured in triplicate for all primers. For beta-globin,
701 primers were bglobin-f and bglobin-r. Cycling conditions were 1x 95°C for 5'; 35x 95°C for
702 10'', 65°C for 20'' (50°C for beta-globin) and 72°C for 30''. Relative concentrations of total
703 DNA (Late RT), 2-LTR circles and integrated viral DNA were calculated relative to beta-globin
704 using the ΔCt method. The primers used are listed in **Table 3**.
705
706 Western Blotting
707 0.5 to 1 million cells were lysed in 100 μL of RIPA buffer (50mM Tris HCl, 150mM NaCl,
708 0.1% SDS, 0.5% DOC, 1% NP-40, Protease inhibitor (Roche; 1187358001)). Lysis was
709 performed on ice for 30'. Lysates were cleared by centrifugation at 8000 g for 8 minutes at 4°C,
710 20 μl of Laemmli 6x (12% SDS, 30% Glycerol, 0.375M Tris-HCl pH 6.8, 30% 2-
711 mercaptoehtanol, 1% bromophenol blue) was added and samples were boiled at 95°C for 15'.
712 Cellular protein lysates were resolved on Criterion or 4%–20% Bio-Rad precast SDS-PAGE
713 gels and transferred to PVDF membranes (Bio-Rad). Membranes were saturated and proteins
714 were blotted with antibodies in 5% non-fat dry milk, PBS 0.1% Tween buffer. ECL signal

715 generated via Clarity Western ECL substrate (Bio-Rad) was recorded on the ChemiDoc-XRS
716 or ChemiDoc Touch Bio-Rad Imager. Data was analyzed and quantified with the Image Lab
717 software (Bio-Rad). The antibodies used in this study are listed in **Table 4**.
718
719 Live Confocal Imaging
720 For live imaging, HeLa cells were plated either in a glass bottom FuoroDish (World Precision
721 Instruments) or in a glass-bottom Cellview Cell Culture Dish with 4 compartments (Greiner
722 Bio-One), on the day prior to experiments. One hour before imaging, cells were incubated with
723 1 µM of SiR-DNA (Tebu Bio), directly in the culture medium, at 37°C. Images of cells were
724 acquired with a Leica DmI8 inverted microscope equipped with an SP8 confocal unit using a
725 20x dry objective (NA=0.75, pixel size was fixed to 0.284 µm). Imaging was performed in an
726 on-stage incubator chamber at 37°C, with 5% CO_2. An image per condition was taken every 2
727 minutes, unless specified otherwise.
728 Image analysis was performed using Fiji software (Schindelin et al., 2012). For chromatin
729 dynamics analysis, a homemade macro was first used to do segmentation of each nucleus on
730 the movie and identify them using the 3D object counter. Particle Image Velocimetry (PIV)
731 analysis was then performed on SiR-DNA staining using the PIV plug-in (Tseng et al., 2012).
732 PIV is a basic optic flow analysis, that divides each image of a stack in small clusters of pixels
733 (interrogation windows) and measures the displacement of each cluster between pairs of
734 consecutive frames. The cross-correlation then generates a pattern of "movements" within the
735 nucleus that are color-coded based on the amplitude of the vector corresponding to the
736 displacement of each cluster. An in-house script was used to first align each individual nucleus,
737 then measure and average SiR-DNA displacements over the ten first time points. Red shades
738 indicate higher amplitudes of displacement while violets correspond to quasi-immobile
739 clusters. For nuclear rotation analysis, a macro was used to measure rotation angles across the

740 first 30 frames. Briefly, individual nuclei were first aligned using a translation transformation
741 of the MultiStackReg plug-in (Brad Busse, Stanford), then they were aligned using the rotation
742 transformation and the transformation was applied to a reference image containing 2 fixed
743 points (one at the center and one on the edge) to measure the rotation. A threshold of 1
744 degree/minute was used to define rotating nuclei. The percentage of rotation time and the
745 average velocity was then computed.
746
747 Confocal Immunofluorescence Imaging
748 For immunofluorescence, HeLa cells were grown overnight onto 12 mm glass coverslips
749 (Thermo Scientific) placed in 6-well plates. Cells were fixed with 4% PFA for 20 minutes at
750 room temperature. Coverslips were washed multiple times with PBS and quenched with 0.1M
751 Glycine in PBS(Life Technologies) for 10 minutes at room temperature. Coverslips were then
752 blocked with PBS, 0.2% (w/v) BSA (Euromedex), 0.05% (w/v) Saponin from quillaja bark
753 (SIGMA) for 30 minutes at room temperature. Cells were stained overnight with anti-NUP153
754 antibody at 2 µg/mL (1:50 dilution) or with Normal Rabbit IgG Isotype Control at
755 corresponding concentration of the primary antibody, in PBS, 0.2% (w/v) BSA, 0.05% (w/v)
756 Saponin + 10% goat serum (Sigma), at 4°C in a humidified chamber. The following day, cells
757 were washed multiple times and incubated with the secondary antibody Alexa Fluor 546 goat
758 anti-rabbit IgG (H+L) (Invitrogen; 1:200 dilution in PBS-BSA-Saponin) in the presence of 1
759 µM of SiR-DNA for 2 hours in the dark, at room temperature. Coverslips were washed multiple
760 times in PBS-BSA-Saponin and finally rinsed once in distilled water. Coverslips were mounted
761 onto glass slides using Fluoromount G (eBioscience) mounting medium. The slides were finally
762 dried at 37°C for 1h and stored at 4°C. Cells were imaged with a Leica DmI8 inverted
763 microscope equipped with an SP8 confocal unit using an oil immersion 63x objective (NA=1.4)
764 with applied Type F Immersion Liquid (Leica).

765

766 Fluorescence Recovery After Photobleaching

767 Cells were seeded at 2.5 x 10^5 cells/dish in a glass bottom FuoroDish (World Precision
768 Instruments) on the day prior to the experiment. Cells were imaged with a Leica DmI8 inverted
769 microscope equipped with an SP8 confocal unit using a 20x dry objective (NA=0.75). Imaging
770 was performed in an on-stage incubator chamber at 37°C, with 5% CO_2. Two independent
771 modules were used in a sequential manner: one for bleaching, one for imaging the signal
772 recovery. During the application of the bleaching module, the 488 laser was focused at an
773 intensity of 5% and with a gain of 0.1% on to an area within the nucleus of each cell at maximum
774 zoom for 20 seconds. Immediately afterwards, the first sequence was manually cancelled, the
775 resolution was optimized, imaging area was restored to the whole cell for the second sequence.
776 The laser power was set for optimal imaging level and images of the whole cell were acquired
777 for 3 min circa at the rate of one image every 2.2 seconds.

778

779 Intracellular staining for flow cytometry

780 Cell surface staining was performed in PBS, 1% BSA (Euromedex), 1mM EDTA (GIBCO),
781 0.01% NaN3 (AMRESCO) (FACS Buffer) at 4°C. Viability staining (Live-Dead) with Fixable
782 Viability Dye eFluor 780 was performed in PBS at 4°C. Cells were resuspended in FACS
783 Buffer prior to final acquisition. Intracellular staining of γH2AX was performed using the
784 FOXP3/Transcription Factor Staining Buffer Set (eBioscience) as per manufacturer's protocol.
785 Cells were resuspended in FACS Buffer prior to final acquisition. All flow cytometry
786 acquisitions were performed on the FACSVerse (BD) using the FACSSuite software (BD) and
787 analyzed on FlowJo v10. The antibodies used are listed in **Table 4**.

788

789 Electron Microscopy

790 Cells were seeded at 5 x 10^4 cells/well in a 24w plate onto sterile 12 mm glass coverslips
791 (Thermo Scientific) and left to adhere overnight. The following morning, cells were washed in
792 PBS and were fixed using 2% glutaraldehyde in 0.1 M cacoldylate buffer, pH 7.4 for 1h, post
793 fixed for 1h with 2% buffered osmium tetroxide, dehydrated in a graded series of ethanol
794 solution, and then embedded in epoxy resin. Images were acquired with a digital camera
795 Quemesa (SIS) mounted on a Tecnai Spirit transmission electron microscope (FEI Company)
796 operated at 80kV.
797
798 Micropipette aspiration microscopy
799 Prior to harvest, HeLa cell lines were incubated with 1µM SiR-DNA dye from Tebu Bio for
800 1h30 at 37°C in cell culture medium. Cells were washed, harvested and resuspended at a
801 concentration of 5x10^6 cells/mL in sterile 3% BSA in PBS-0.2% FBS. Cells were subjected to
802 the experimental conditions as described (Davidson et al., 2019).
803
804 Microarray Gene Expression (Affymetrix)
805 Total RNA was extracted from 10^6 HeLa cells using NucleoSpin RNA and adjusted to 50
806 ng/µL. A WT PLUS amplification and labeling protocol was conducted with 100 ng of total
807 RNA. Samples passed the quality control with a high score. The Affymetrix analysis was
808 performed by the NGS platform at Institut Curie using the Human Gene 2.0 ST chip. Human
809 Gene 2.0ST array were scanned using a Genechip 7G scanner, according to the supplier's
810 protocol. Micro-array analyses were processed with R using packages from Bioconductor. The
811 quality control was performed using ArrayQualityMetrics package without detecting any
812 outlier among the experiment. Data was normalized using the Robust Multi-Array Average
813 algorithm from the Oligo package. Annotation of the probes was done using the hugene20
814 annotation data (chip hugene20sttranscriptcluster) from Bioconductor. Differential gene-

815 expression analysis was performed with Limma. The accession number for the raw data files is
816 NCBI GEO: GSE162019.
817
818 Statistical Analysis
819 Statistical analyses were performed in Prism 7 or 8 (GraphPad Software) as indicated in the
820 figure legends.
821

822

823 **Supplementary Tables**

824

825 Table 1: Plasmids used in this study

Plasmid Name	Purpose	Insert/ Target/ Components	Reporter / Selection	Source or Identifier
pTRIP-SFFV-tagBFP-2A	Overexpression	/	BFP	(Cerboni et al., 2017)
pTRIP-SFFV-TagRFP657-2A	Overexpression	/	RFP657	This study
pTRIP-SFFV-EGFP	Overexpression	/	GFP	(Lahaye et al., 2016)
pTRIP-CMV-EGFP-2A	Overexpression	/	GFP	
pTRIP-SFFV-tagBFP-2A-SUN1	Overexpression	SUN1	BFP	This study (MGC cDNA cloneID: 40148817)
pTRIP-SFFV-tagBFP-2A-NtSUN2	Overexpression	SUN2	BFP	This study
pTRIP-SFFV-tagBFP-2A-SUN1 Dharmacon (1-298)-ntSUN2 (220-717)	Overexpression	SUN1-SUN2	BFP	This study

pTRIP-SFFV-tagBFP-2A-NtSUN2 (1-219)-SUN1 Dharmacon (299-785)	Overexpression	SUN2-SUN1	BFP	This study
pTRIP-SFFV-TagRFP657-2A-SUN1 Dharmacon	Overexpression	SUN1	RFP657	This study (MGC cDNA cloneID: 40148817
pTRIP-SFFV-TagRFP657-2A-ntSUN2	Overexpression	SUN2	RFP657	This Study
pTRIP-SFFV-EGFP-SR-KASH	Overexpression	SR-KASH	GFP	This study
pLKO1puro-shLACZ shRNA sequence: GCGATCGTAATCACCCGAGTG	Knock-down	LacZ	Puromycin	pLKO.1 clone ID TRCN0000072229
pLKO.1-Puro-LMNA sh2 shRNA sequence: GAAGCAACTTCAGGATGAGAT	Knock-down	Lamin A/C	Puromycin	pLKO.1 clone ID TRCN0000061835
pLKO.1-Puro-LMNB2 sh5 shRNA sequence:	Knock-down	Lamin B2	Puromycin	pLKO.1 clone ID TRCN0000072422

CTACAAGTTCACGCC CAAGTA				
pCMV-VSVG	Expression	VSV-G	/	(Manel et al., 2010)
psPAX2	Packaging vector	/	/	(Manel et al., 2010)
HIVGFP (NL4-3 strain)	Infection	Vif-, Vpr-, Vpu-, Env-, Nef-	GFP in Nef	(Manel et al., 2010)
HIVGFP N74D	Infection	Vif-, Vpr-, Vpu-, Env-, Nef-, CA mutation N74D	GFP in Nef	(Lahaye et al., 2016)
HIVGFP env-nef-	Infection	Vif+, Vpr+, Vpu+, Env-, Nef-	GFP in Nef	This study
HIVGFP env- nef- vpr-	Infection	Vif+, Vpr-, Vpu+, Env-, Nef-	GFP in Nef	This study
HIV-mTagBFP2 (NL4-3 strain)	Infection	Vif-, Vpr-, Vpu-, Env-, Nef-	BFP in Nef	This study

HIV-2 ROD9 Δenv Δnef mTagBFP2+	Infection	Vif+, Vpr+, Vpx+, Env-, Nef-	BFP in Nef	This study
HIV-2 ROD9 Δenv Δnef GFP	Infection	Vif+, Vpr+, Vpx+, Env-, Nef-	GFP in Nef	(Manel et al., 2010)
pSIV3+	Helper plasmid		/	(Mangeot et al., 2000)

826

827 Table 2: Drugs used in cell culture in this study

Name	**Description**	**Cat. Reference**	**Company**	**Final Concentration**
Cyclosporin A	Inhibits CypA-CA interaction	S2286	Selleckchem	2 µM
AZT	Reverse transcriptase inhibitor	A2169	Sigma	24 µM
NVP	Reverse transcriptase inhibitor	SML0097	Sigma	10 µM
Etoposide	Topoisomerase II inhibitor	E1383	Sigma	5, 50 or 500 µM
Q-VD-Oph	Pan-caspase inhibitor	S7311	Selleckchem	50 µM
AZD6738	ATR inhibitor	S7693	Selleckchem	1 µM

DMSO	Diluent	BDH1115	VWR Chemicals	adjusted

828

829

830 Table 3: Primers used for HIV DNA species Real Time Quantitiative PCR

Strain	**Amplification**	**Primer name**	**Sequence**	**Annealing**
Human	Beta-globin	bglobin-f	CCCTTGGACCCAGAGGTTCT	50°C
Human	Beta-globin	bglobin-r	CGAGCACTTTCTTGCCATGA	50°C
HIV-1	Total DNA (Late RT)	hiv1-3'U3-fwd	GCATGGAATGGATGACCCTGAGA	65°C
HIV-1	Total DNA (Late RT)	hiv1-psi-rev2	CGTCGAGAGATCTCCTCT GGCTTTA	65°C
HIV-1	2-LTR circles	Junct4 -fwd	CAGTGTGGAAAATCTCTA GCAGTACTG	65°C
HIV-1	2-LTR circles	hiv1-psi-rev2	CGTCGAGAGATCTCCTCT GGCTTTA	65°C
HIV-1	Integrated DNA round 1	alu1	GCCTCCCAAAGTGCT GGGATTACAG	65°C
HIV-1	Integrated DNA round 1	hiv1-psi-rev2	CGTCGAGAGATCTCCTCT GGCTTTA	65°C

HIV-1	Integrated DNA round 2	hiv1-f2	CTGGGAGCTCTCTGGCTAACTA	65°C
HIV-1	Integrated DNA round 2	hiv1-r2	AACAGACGGGCACACACTACTT	65°C
HIV-2	Total DNA (Late RT)	hiv2-3'U3-fwd	GAAGGGATGTTTT ACCATTTAGTTA	65°C
HIV-2	Total DNA (Late RT)	hiv2-psi-rev	GTTCCAAGACTTCTCAGTCTTCTTC	65°C
HIV-2	2-LTR circles	hiv2-R-fwd	GTTCTCTCCAGCACTAGCAGGTA	65°C
HIV-2	2-LTR circles	hiv2-3'U3-rev	TAACTAAATGGTA AAACATCCCTTC	65°C
HIV-2	Integrated DNA round 1	alu1	GCCTCCCAAAGTGCT GGGATTACAG	65°C
HIV-2	Integrated DNA round 1	hiv2-r1	AAGGGTCCTAACAGACCAGGGTCT	65°C
HIV-2	Integrated DNA round 2	hiv2-f2	GCAGGTAGAGCCTGGGTGTTC	65°C
HIV-2	Integrated DNA round 2	hiv2-r2	CAGGCGGCGACTAGGAGAGAT	65°C

831

832

833 Table 4: Antibodies used in this study for Western Blot, Confocal Imaging and Flow

834 Cytometry

Antibody target	Cat. Reference	Company	Application
Actin	MAB1501 Clone C4	Sigma	WB (1:5000)
Vinculin	V9264	Sigma	WB (1:5000)
SUN1	ab124770	Abcam	WB (1:1000)
SUN2	HPA001209	Atlas antibodies	WB (1:1000)
SUN2	ABT272	Millipore	WB (1:1000)
Lamin A/C	SAB4200236	Sigma	WB (1:1000)
Lamin B2	ab8983 clone LN43	Abcam	WB (1:1000)
NUP153	HPA027896	Sigma	IF (1:50)
SiR-DNA staining	SC007	Tebu Bio	Live imaging (1µM)
H2AX p-S139	562377 Clone N1-431	BD	Coupled to PE; FACS (1:100)
Mouse IgG1 κ isotype control	554680 Clone MOPC-21	BD	Coupled to PE; FACS (1:100)
Rabbit-IgG (H+L)	A-11010	Invitrogen	Alexa Fluor 546 for IF (1:200)
Rabbit-IgG	7074S	Ozyme	Conjugated to HRP for WB (1:10000)
Mouse IgG	7076S	Ozyme	Conjugated to HRP for WB (1:10000)

835

836 **References**

837 Ariumi, Y., Turelli, P., Masutani, M., and Trono, D. (2005). DNA Damage Sensors ATM,
838 ATR, DNA-PKcs, and PARP-1 Are Dispensable for Human Immunodeficiency Virus Type 1
839 Integration. J. Virol. *79*, 2973–2978.

840 Bhargava, A., Lahaye, X., and Manel, N. (2018). Let me in: Control of HIV nuclear entry at
841 the nuclear envelope. Cytokine Growth Factor Rev. *40*, 59–67.

842 Braaten, D., and Luban, J. (2001). Cyclophilin A regulates HIV-1 infectivity, as demonstrated
843 by gene targeting in human T cells. EMBO J *20*, 1300–1309.

844 Burke, B., and Stewart, C.L. (2013). The nuclear lamins: flexibility in function. Nat. Rev.
845 Mol. Cell Biol. *14*, 13–24.

846 Cerboni, S., Jeremiah, N., Gentili, M., Gehrmann, U., Conrad, C., Stolzenberg, M.C., Picard,
847 C., Neven, B., Fischer, A., Amigorena, S., et al. (2017). Intrinsic antiproliferative activity of
848 the innate sensor STING in T lymphocytes. J Exp Med.

849 Davidson, P.M., Fedorchak, G.R., Mondésert-Deveraux, S., Bell, E.S., Isermann, P., Aubry,
850 D., Allena, R., and Lammerding, J. (2019). High-throughput microfluidic micropipette
851 aspiration device to probe time-scale dependent nuclear mechanics in intact cells. Lab. Chip
852 *19*, 3652–3663.

853 De Iaco, A., and Luban, J. (2014). Cyclophilin A promotes HIV-1 reverse transcription but its
854 effect on transduction correlates best with its effect on nuclear entry of viral cDNA.
855 Retrovirology *11*, 11.

856 DeHart, J.L., Andersen, J.L., Zimmerman, E.S., Ardon, O., An, D.S., Blackett, J., Kim, B.,
857 and Planelles, V. (2005). The Ataxia Telangiectasia-Mutated and Rad3-Related Protein Is
858 Dispensable for Retroviral Integration. J. Virol. *79*, 1389–1396.

859 Dharan, A., Bachmann, N., Talley, S., Zwikelmaier, V., and Campbell, E.M. (2020). Nuclear
860 pore blockade reveals that HIV-1 completes reverse transcription and uncoating in the
861 nucleus. Nat. Microbiol. *5*, 1088–1095.

862 Donahue, D.A., Amraoui, S., di Nunzio, F., Kieffer, C., Porrot, F., Opp, S., Diaz-Griffero, F.,
863 Casartelli, N., and Schwartz, O. (2016). SUN2 Overexpression Deforms Nuclear Shape and
864 Inhibits HIV. J. Virol. *90*, 4199–4214.

865 Donahue, D.A., Porrot, F., Couespel, N., and Schwartz, O. (2017). SUN2 Silencing Impairs
866 CD4 T Cell Proliferation and Alters Sensitivity to HIV-1 Infection Independently of
867 Cyclophilin A. J. Virol. *91*.

868 Ebina, H., Kanemura, Y., Suzuki, Y., Urata, K., Misawa, N., and Koyanagi, Y. (2012).
869 Integrase-independent HIV-1 infection is augmented under conditions of DNA damage and
870 produces a viral reservoir. Virology *427*, 44–50.

871 Foote, K.M., Nissink, J.W.M., McGuire, T., Turner, P., Guichard, S., Yates, J.W.T., Lau, A.,
872 Blades, K., Heathcote, D., Odedra, R., et al. (2018). Discovery and Characterization of
873 AZD6738, a Potent Inhibitor of Ataxia Telangiectasia Mutated and Rad3 Related (ATR)
874 Kinase with Application as an Anticancer Agent. J. Med. Chem. *61*, 9889–9907.

875 Goh, W.C., Rogel, M.E., Kinsey, C.M., Michael, S.F., Fultz, P.N., Nowak, M.A., Hahn, B.H.,
876 and Emerman, M. (1998). HIV-1 Vpr increases viral expression by manipulation of the cell
877 cycle: a mechanism for selection of Vpr in vivo. Nat. Med. *4*, 65–71.

878 Gonzalo, S. (2014). DNA Damage and Lamins. In Cancer Biology and the Nuclear Envelope,

879 E.C. Schirmer, and J.I. de las Heras, eds. (New York, NY: Springer New York), pp. 377–399.

880 Ji, J.Y., Lee, R.T., Vergnes, L., Fong, L.G., Stewart, C.L., Reue, K., Young, S.G., Zhang, Q.,
881 Shanahan, C.M., and Lammerding, J. (2007). Cell Nuclei Spin in the Absence of Lamin B1. J.
882 Biol. Chem. *282*, 20015–20026.

883 Kidiyoor, G.R., Li, Q., Bastianello, G., Bruhn, C., Giovannetti, I., Mohamood, A.,
884 Beznoussenko, G.V., Mironov, A., Raab, M., Piel, M., et al. (2020). ATR is essential for
885 preservation of cell mechanics and nuclear integrity during interstitial migration. Nat.
886 Commun. *11*, 4828.

887 Koyama, T., Sun, B., Tokunaga, K., Tatsumi, M., and Ishizaka, Y. (2013). DNA damage
888 enhances integration of HIV-1 into macrophages by overcoming integrase inhibition.
889 Retrovirology *10*, 21.

890 Kumar, A., Mazzanti, M., Mistrik, M., Kosar, M., Beznoussenko, G.V., Mironov, A.A.,
891 Garrè, M., Parazzoli, D., Shivashankar, G.V., Scita, G., et al. (2014). ATR mediates a
892 checkpoint at the nuclear envelope in response to mechanical stress. Cell *158*, 633–646.

893 Lahaye, X., Satoh, T., Gentili, M., Cerboni, S., Conrad, C., Hurbain, I., El Marjou, A.,
894 Lacabaratz, C., Lelievre, J.D., and Manel, N. (2013). The capsids of HIV-1 and HIV-2
895 determine immune detection of the viral cDNA by the innate sensor cGAS in dendritic cells.
896 Immunity *39*, 1132–1142.

897 Lahaye, X., Satoh, T., Gentili, M., Cerboni, S., Silvin, A., Conrad, C., Ahmed-Belkacem, A.,
898 Rodriguez, E.C., Guichou, J.-F., Bosquet, N., et al. (2016). Nuclear Envelope Protein SUN2
899 Promotes Cyclophilin-A-Dependent Steps of HIV Replication. Cell Rep. *15*, 879–892.

900 Lammerding, J., Schulze, P.C., Takahashi, T., Kozlov, S., Sullivan, T., Kamm, R.D., Stewart,
901 C.L., and Lee, R.T. (2004). Lamin A/C deficiency causes defective nuclear mechanics and
902 mechanotransduction. J. Clin. Invest. *113*, 370–378.

903 Lawrence, K.S., Tapley, E.C., Cruz, V.E., Li, Q., Aung, K., Hart, K.C., Schwartz, T.U., Starr,
904 D.A., and Engebrecht, J. (2016). LINC complexes promote homologous recombination in part
905 through inhibition of nonhomologous end joining. J. Cell Biol. *215*, 801–821.

906 Lei, K., Zhang, X., Ding, X., Guo, X., Chen, M., Zhu, B., Xu, T., Zhuang, Y., Xu, R., and
907 Han, M. (2009). SUN1 and SUN2 play critical but partially redundant roles in anchoring
908 nuclei in skeletal muscle cells in mice. Proc Natl Acad Sci U A *106*, 10207–10212.

909 Lei, K., Zhu, X., Xu, R., Shao, C., Xu, T., Zhuang, Y., and Han, M. (2012). Inner nuclear
910 envelope proteins SUN1 and SUN2 play a prominent role in the DNA damage response. Curr
911 Biol *22*, 1609–1615.

912 Liu, Q., Pante, N., Misteli, T., Elsagga, M., Crisp, M., Hodzic, D., Burke, B., and Roux, K.J.
913 (2007). Functional association of Sun1 with nuclear pore complexes. J Cell Biol *178*, 785–
914 798.

915 Lottersberger, F., Karssemeijer, R.A., Dimitrova, N., and de Lange, T. (2015). 53BP1 and the
916 LINC Complex Promote Microtubule-Dependent DSB Mobility and DNA Repair. Cell *163*,
917 880–893.

918 Luo, X., Yang, W., and Gao, G. (2018). SUN1 Regulates HIV-1 Nuclear Import in a Manner
919 Dependent on the Interaction between the Viral Capsid and Cellular Cyclophilin A. J. Virol.
920 *92*, e00229-18.

921 Manel, N., Hogstad, B., Wang, Y., Levy, D.E., Unutmaz, D., and Littman, D.R. (2010). A
922 cryptic sensor for HIV-1 activates antiviral innate immunity in dendritic cells. Nature *467*,

923 214–217.

924 Mangeot, P.E., Negre, D., Dubois, B., Winter, A.J., Leissner, P., Mehtali, M., Kaiserlian, D.,
925 Cosset, F.L., and Darlix, J.L. (2000). Development of minimal lentivirus vectors derived from
926 simian immunodeficiency virus (SIVmac251) and their use for gene transfer into human
927 dendritic cells. J Virol *74*, 8307–8315.

928 Mlcochova, P., Caswell, S.J., Taylor, I.A., Towers, G.J., and Gupta, R.K. (2018). DNA
929 damage induced by topoisomerase inhibitors activates SAMHD1 and blocks HIV-1 infection
930 of macrophages. EMBO J. *37*, 50–62.

931 de Noronha, C.M., Sherman, M.P., Lin, H.W., Cavrois, M.V., Moir, R.D., Goldman, R.D.,
932 and Greene, W.C. (2001). Dynamic disruptions in nuclear envelope architecture and integrity
933 induced by HIV-1 Vpr. Science *294*, 1105–1108.

934 Oza, P., Jaspersen, S.L., Miele, A., Dekker, J., and Peterson, C.L. (2009). Mechanisms that
935 regulate localization of a DNA double-strand break to the nuclear periphery. Genes Dev. *23*,
936 912–927.

937 Procter, D.J., Banerjee, A., Nukui, M., Kruse, K., Gaponenko, V., Murphy, E.A., Komarova,
938 Y., and Walsh, D. (2018). The HCMV Assembly Compartment Is a Dynamic Golgi-Derived
939 MTOC that Controls Nuclear Rotation and Virus Spread. Dev. Cell *45*, 83-100.e7.

940 Ranade, D., Pradhan, R., Jayakrishnan, M., Hegde, S., and Sengupta, K. (2019). Lamin A/C
941 and Emerin depletion impacts chromatin organization and dynamics in the interphase nucleus.
942 BMC Mol. Cell Biol. *20*, 11.

943 Rello-Varona, S., Gámez, A., Moreno, V., Stockert, J.C., Cristóbal, J., Pacheco, M., Cañete,
944 M., Juarranz, Á., and Villanueva, Á. (2006). Metaphase arrest and cell death induced by
945 etoposide on HeLa cells. Int. J. Biochem. Cell Biol. *38*, 2183–2195.

946 Roshal, M., Kim, B., Zhu, Y., Nghiem, P., and Planelles, V. (2003). Activation of the ATR-
947 mediated DNA Damage Response by the HIV-1 Viral Protein R. J. Biol. Chem. *278*, 25879–
948 25886.

949 Schaller, T., Ocwieja, K.E., Rasaiyaah, J., Price, A.J., Brady, T.L., Roth, S.L., Hué, S.,
950 Fletcher, A.J., Lee, K., KewalRamani, V.N., et al. (2011). HIV-1 Capsid-Cyclophilin
951 Interactions Determine Nuclear Import Pathway, Integration Targeting and Replication
952 Efficiency. PLoS Pathog. *7*, e1002439.

953 Schaller, T., Bulli, L., Pollpeter, D., Betancor, G., Kutzner, J., Apolonia, L., Herold, N., Burk,
954 R., and Malim, M.H. (2017). Effects of Inner Nuclear Membrane Proteins SUN1/UNC-84A
955 and SUN2/UNC-84B on the Early Steps of HIV-1 Infection. J. Virol. *91*, e00463-17, e00463-
956 17.

957 Schindelin, J., Arganda-Carreras, I., Frise, E., Kaynig, V., Longair, M., Pietzsch, T.,
958 Preibisch, S., Rueden, C., Saalfeld, S., Schmid, B., et al. (2012). Fiji: an open-source platform
959 for biological-image analysis. Nat Methods *9*, 676–682.

960 Schoggins, J.W., Wilson, S.J., Panis, M., Murphy, M.Y., Jones, C.T., Bieniasz, P., and Rice,
961 C.M. (2011). A diverse range of gene products are effectors of the type I interferon antiviral
962 response. Nature *472*, 481–485.

963 Singh, M., Hunt, C.R., Pandita, R.K., Kumar, R., Yang, C.-R., Horikoshi, N., Bachoo, R.,
964 Serag, S., Story, M.D., Shay, J.W., et al. (2013). Lamin A/C depletion enhances DNA
965 damage-induced stalled replication fork arrest. Mol. Cell. Biol. *33*, 1210–1222.

966 Starr, T.K., Jameson, S.C., and Hogquist, K.A. (2003). Positive and negative selection of T

967 cells. Annu Rev Immunol *21*, 139–176.

968 Sun, W.-W., Jiao, S., Sun, L., Zhou, Z., Jin, X., and Wang, J.-H. (2018). SUN2 Modulates
969 HIV-1 Infection and Latency through Association with Lamin A/C To Maintain the
970 Repressive Chromatin. MBio *9*, e02408-17, /mbio/9/3/mBio.02408-17.atom.

971 Tseng, Q., Duchemin-Pelletier, E., Deshiere, A., Balland, M., Guillou, H., Filhol, O., and
972 Thery, M. (2012). Spatial organization of the extracellular matrix regulates cell-cell junction
973 positioning. Proc. Natl. Acad. Sci. *109*, 1506–1511.

974 Yamashita, M., and Engelman, A.N. (2017). Capsid-Dependent Host Factors in HIV-1
975 Infection. Trends Microbiol. *25*, 741–755.

976 Zimmerman, E.S., Sherman, M.P., Blackett, J.L., Neidleman, J.A., Kreis, C., Mundt, P.,
977 Williams, S.A., Warmerdam, M., Kahn, J., Hecht, F.M., et al. (2006). Human
978 immunodeficiency virus type 1 Vpr induces DNA replication stress in vitro and in vivo. J.
979 Virol. *80*, 10407–10418.

980

981

Figure 1

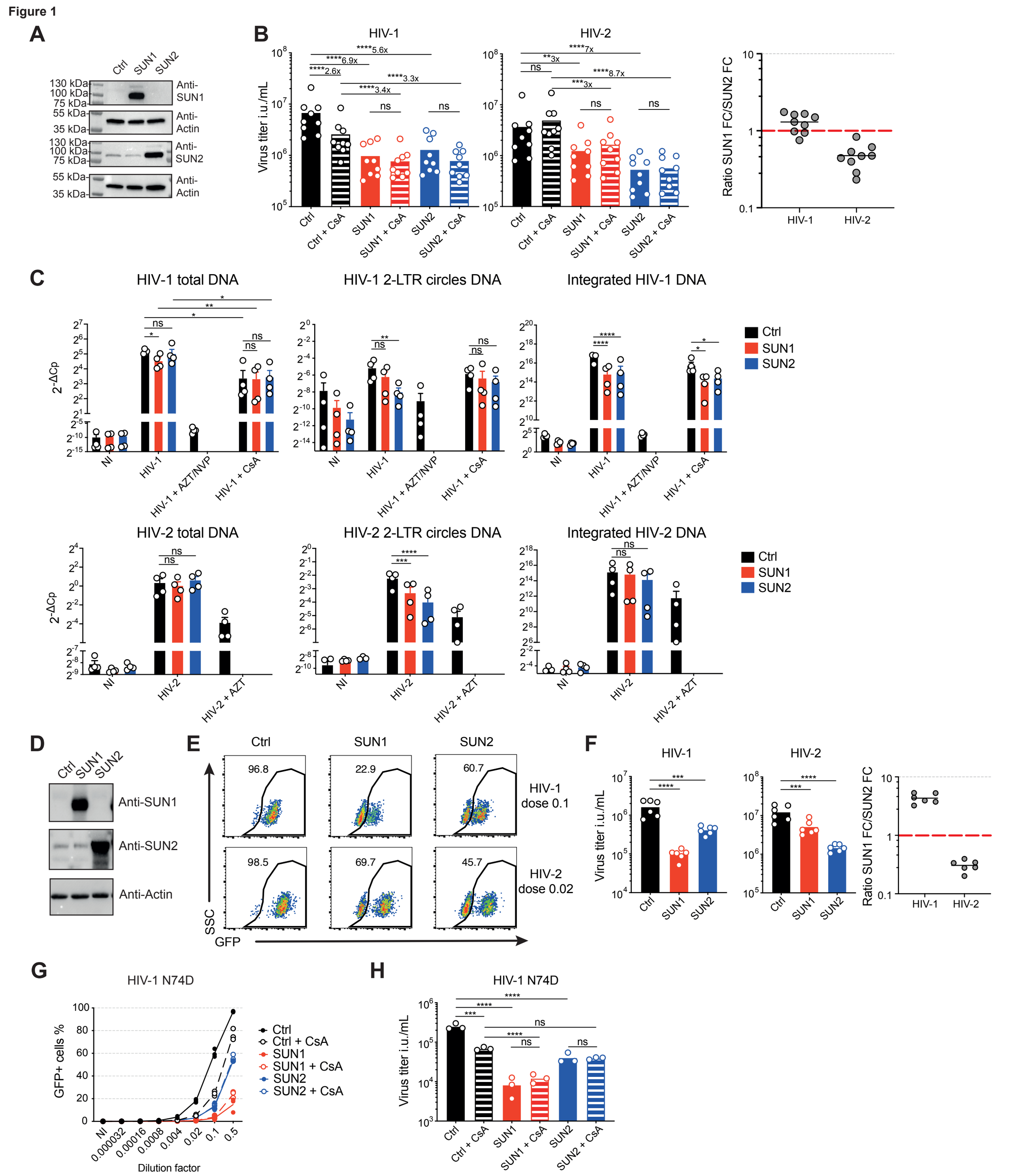
A
Ctrl
SUN1
SUN2
130 kDa
100 kDa
75 kDa
55 kDa
35 kDa
Anti-SUN1
Anti-Actin
Anti-SUN2
B
HIV-1
HIV-2
Virus titer i.u./mL
Ratio SUN1 FC/SUN2 FC
Ctrl
Ctrl + CsA
SUN1
SUN1 + CsA
SUN2
SUN2 + CsA
C
HIV-1 total DNA
HIV-1 2-LTR circles DNA
Integrated HIV-1 DNA
HIV-2 total DNA
HIV-2 2-LTR circles DNA
Integrated HIV-2 DNA
2-ΔCp
NI
HIV-1
HIV-1 + AZT/NVP
HIV-1 + CsA
HIV-2
HIV-2 + AZT
D
Anti-SUN1
Anti-SUN2
Anti-Actin
E
96.8
22.9
60.7
98.5
69.7
45.7
HIV-1 dose 0.1
HIV-2 dose 0.02
SSC
GFP
F
G
HIV-1 N74D
GFP+ cells %
Dilution factor
H

Figure 2

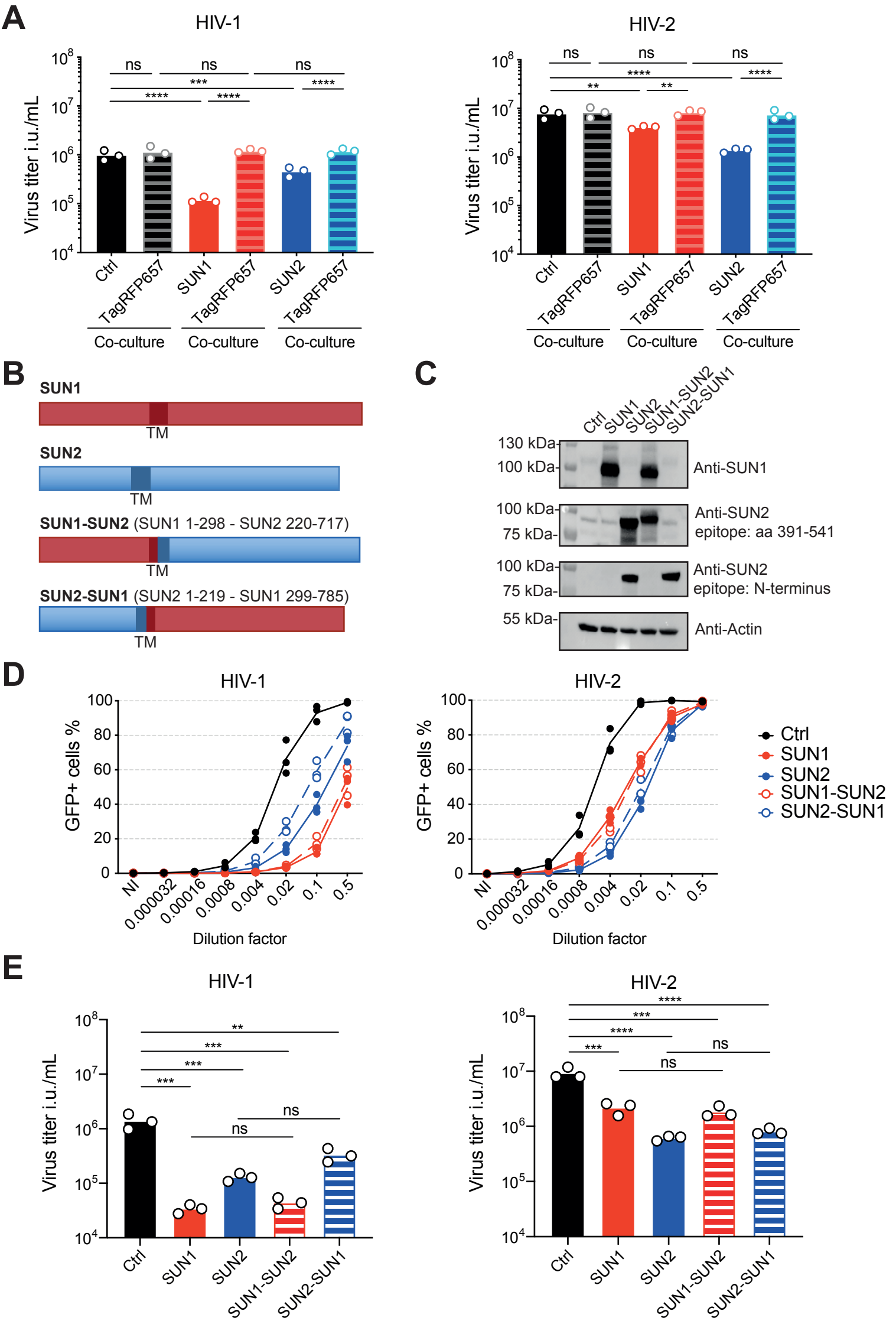
A
HIV-1
HIV-2
Virus titer i.u./mL
ns
**
***
****
Ctrl
TagRFP657
SUN1
SUN2
Co-culture
B
SUN1
SUN2
SUN1-SUN2 (SUN1 1-298 - SUN2 220-717)
SUN2-SUN1 (SUN2 1-219 - SUN1 299-785)
TM
C
Ctrl
SUN1
SUN2
SUN1-SUN2
SUN2-SUN1
130 kDa
100 kDa
75 kDa
55 kDa
Anti-SUN1
Anti-SUN2
epitope: aa 391-541
Anti-SUN2
epitope: N-terminus
Anti-Actin
D
GFP+ cells %
NI
0.000032
0.00016
0.0008
0.004
0.02
0.1
0.5
Dilution factor
Ctrl
SUN1
SUN2
SUN1-SUN2
SUN2-SUN1
E

Figure 3

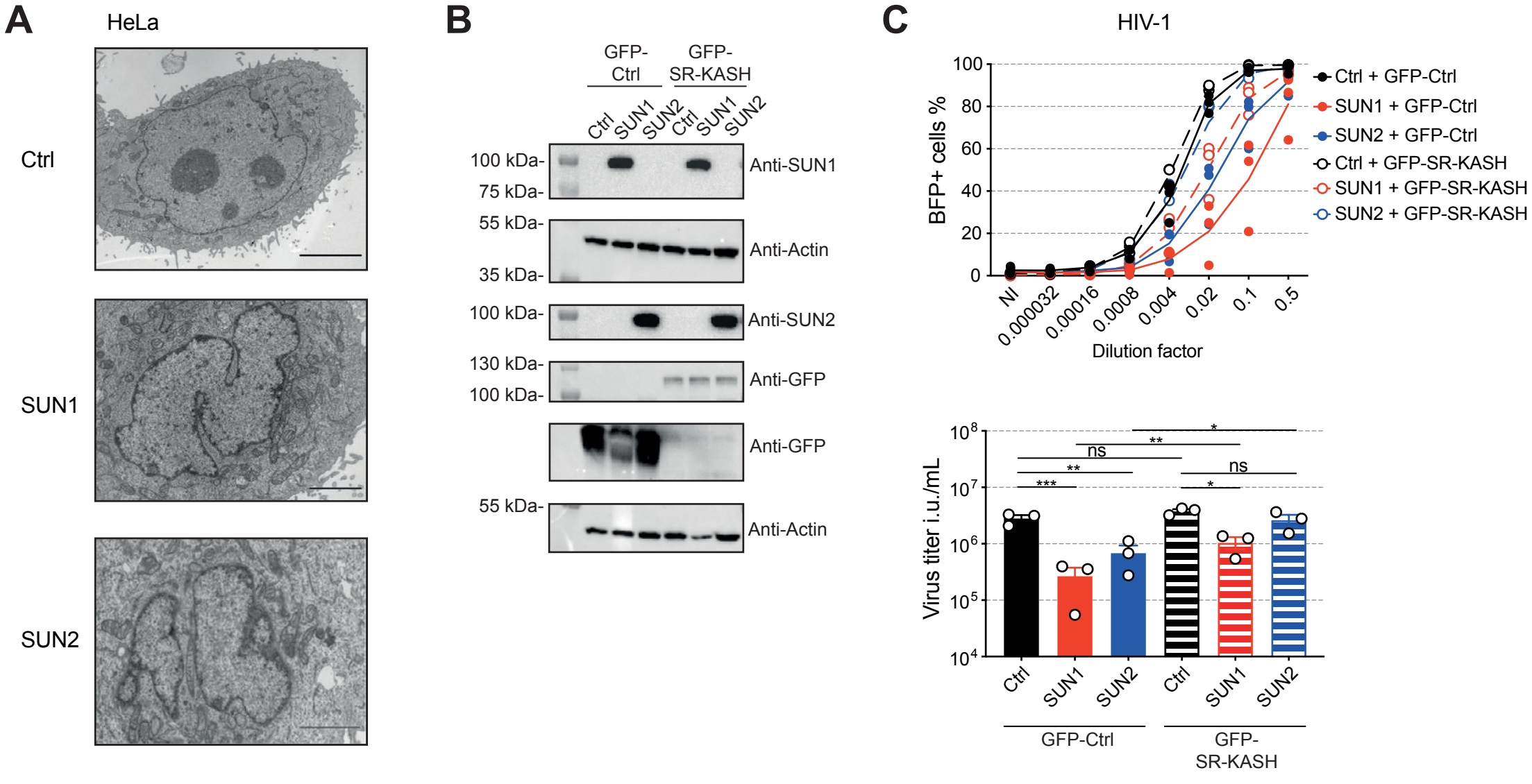
A
HeLa
Ctrl
SUN1
SUN2
B
GFP-Ctrl
GFP-SR-KASH
Ctrl
SUN1
SUN2
Ctrl
SUN1
SUN2
100 kDa-
75 kDa-
Anti-SUN1
55 kDa-
35 kDa-
Anti-Actin
100 kDa-
Anti-SUN2
130 kDa-
100 kDa-
Anti-GFP
Anti-GFP
55 kDa-
Anti-Actin
C
HIV-1
BFP+ cells %
100
80
60
40
20
0
NI
0.000032
0.00016
0.0008
0.004
0.02
0.1
0.5
Dilution factor
Ctrl + GFP-Ctrl
SUN1 + GFP-Ctrl
SUN2 + GFP-Ctrl
Ctrl + GFP-SR-KASH
SUN1 + GFP-SR-KASH
SUN2 + GFP-SR-KASH
Virus titer i.u./mL
10^8
10^7
10^6
10^5
10^4
***
**
ns
*
**
ns
*
Ctrl
SUN1
SUN2
Ctrl
SUN1
SUN2
GFP-Ctrl
GFP-SR-KASH

Figure 4

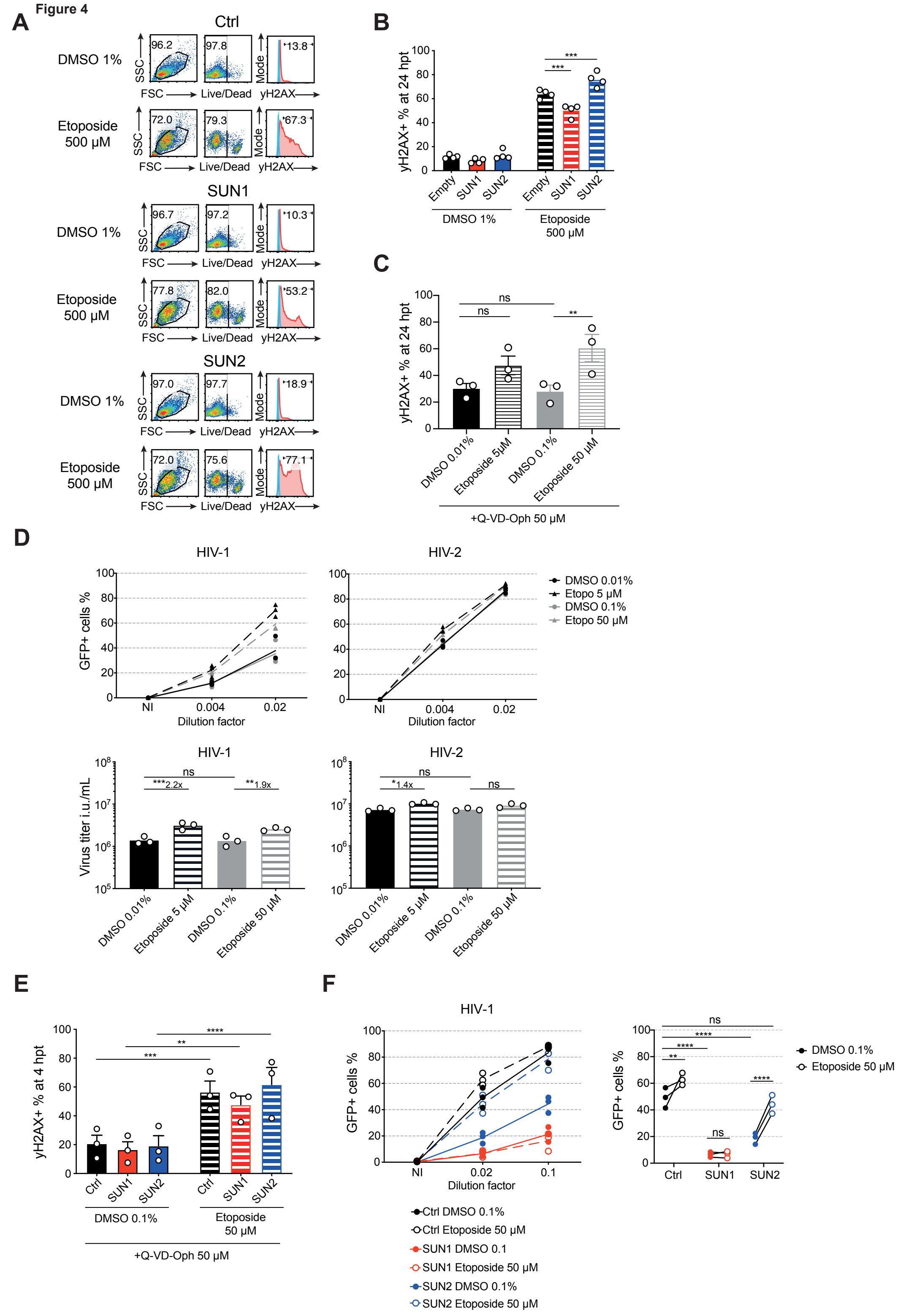
A
Ctrl
DMSO 1%
Etoposide 500 µM
SUN1
SUN2
SSC
FSC
Live/Dead
Mode
yH2AX
96.2
97.8
13.8
72.0
79.3
67.3
96.7
97.2
10.3
77.8
82.0
53.2
97.0
97.7
18.9
72.0
75.6
77.1
B
yH2AX+ % at 24 hpt
Empty
SUN1
SUN2
DMSO 1%
Etoposide 500 µM
C
ns
**
DMSO 0.01%
Etoposide 5µM
DMSO 0.1%
Etoposide 50 µM
+Q-VD-Oph 50 µM
D
HIV-1
HIV-2
GFP+ cells %
NI
0.004
0.02
Dilution factor
DMSO 0.01%
Etopo 5 µM
DMSO 0.1%
Etopo 50 µM
Virus titer i.u./mL
***2.2x
**1.9x
*1.4x
E
yH2AX+ % at 4 hpt
****
**
***
DMSO 0.1%
Etoposide 50 µM
+Q-VD-Oph 50 µM
F
0.1
Ctrl DMSO 0.1%
Ctrl Etoposide 50 µM
SUN1 DMSO 0.1
SUN1 Etoposide 50 µM
SUN2 DMSO 0.1%
SUN2 Etoposide 50 µM

Figure 5

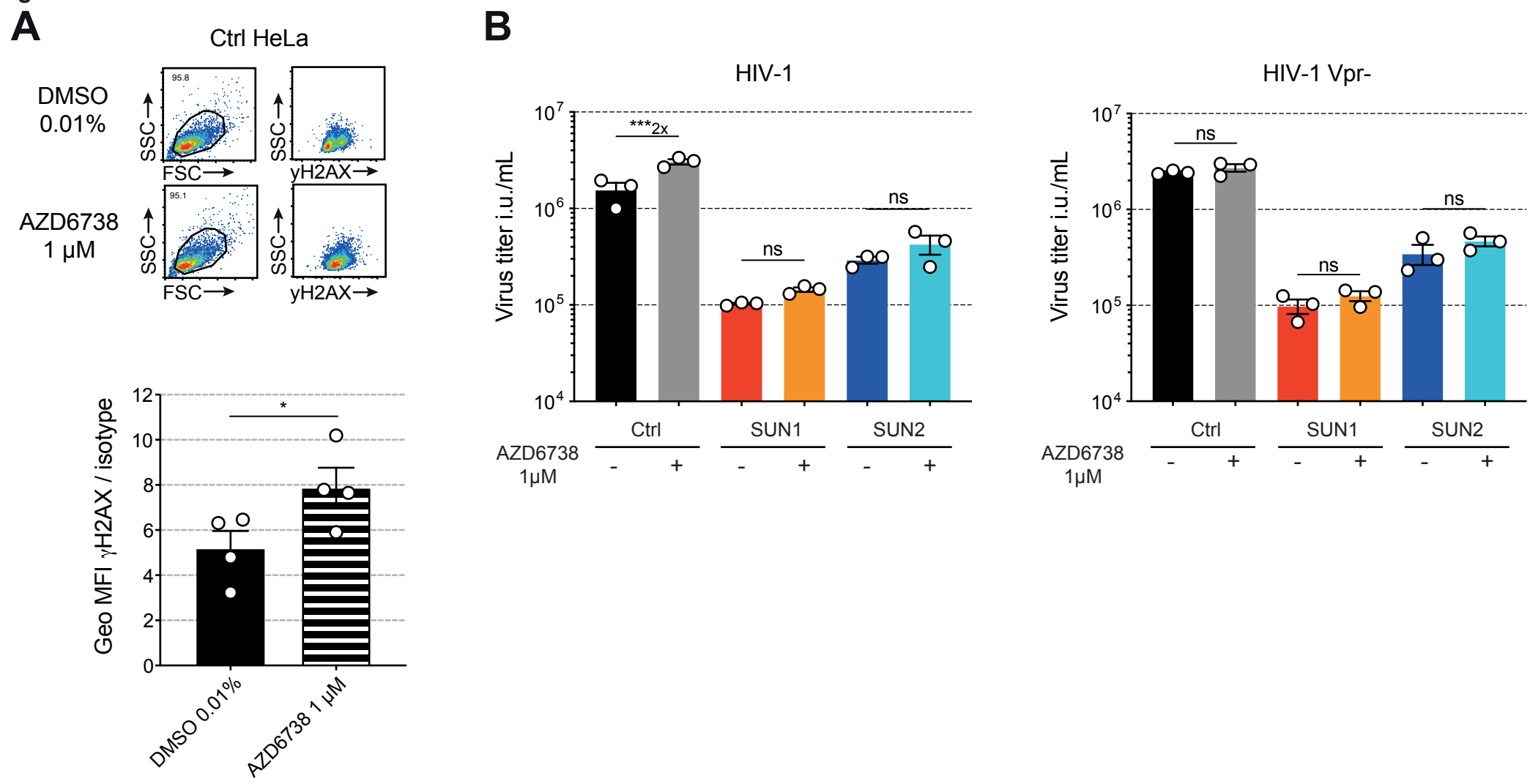
A
Ctrl HeLa
DMSO
0.01%
AZD6738
1 μM
SSC
FSC
yH2AX
95.8
95.1
Geo MFI γH2AX / isotype
*
DMSO 0.01%
AZD6738 1 μM
B
HIV-1
HIV-1 Vpr-
Virus titer i.u./mL
***2x
ns
Ctrl
SUN1
SUN2
AZD6738
1μM
-
+

Figure 6

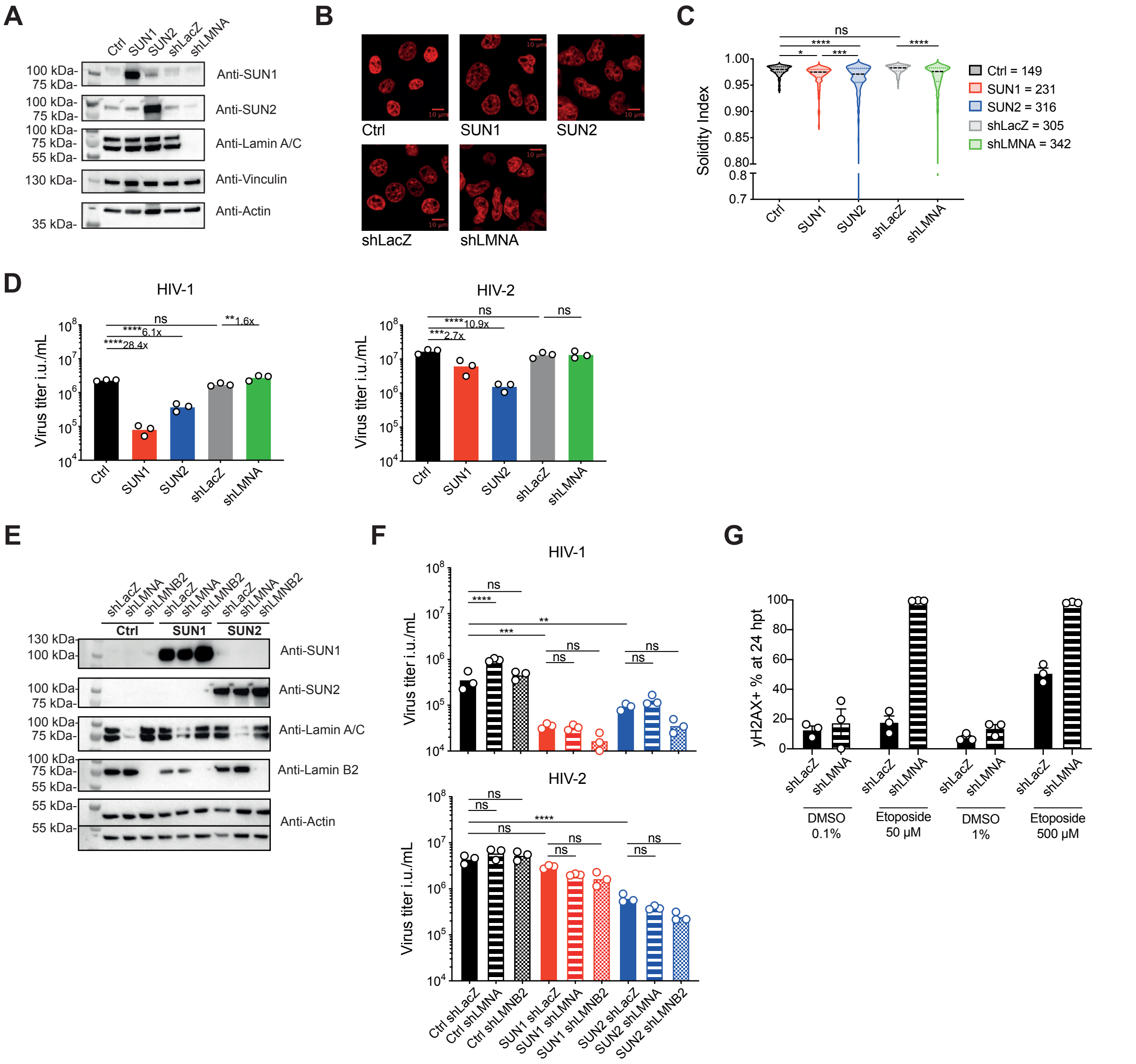
A
Ctrl
SUN1
SUN2
shLacZ
shLMNA
100 kDa-
75 kDa-
55 kDa-
130 kDa-
35 kDa-
Anti-SUN1
Anti-SUN2
Anti-Lamin A/C
Anti-Vinculin
Anti-Actin
B
Ctrl
SUN1
SUN2
shLacZ
shLMNA
10 µm
C
Solidity Index
ns
****
*
***
Ctrl = 149
SUN1 = 231
SUN2 = 316
shLacZ = 305
shLMNA = 342
D
HIV-1
HIV-2
Virus titer i.u./mL
ns
****6.1x
****28.4x
**1.6x
****10.9x
***2.7x
E
shLacZ
shLMNA
shLMNB2
Ctrl
SUN1
SUN2
130 kDa-
100 kDa-
75 kDa-
55 kDa-
Anti-SUN1
Anti-SUN2
Anti-Lamin A/C
Anti-Lamin B2
Anti-Actin
F
HIV-1
HIV-2
Virus titer i.u./mL
ns
****
***
**
Ctrl shLacZ
Ctrl shLMNA
Ctrl shLMNB2
SUN1 shLacZ
SUN1 shLMNA
SUN1 shLMNB2
SUN2 shLacZ
SUN2 shLMNA
SUN2 shLMNB2
G
γH2AX+ % at 24 hpt
shLacZ
shLMNA
DMSO 0.1%
Etoposide 50 µM
DMSO 1%
Etoposide 500 µM

Figure 7

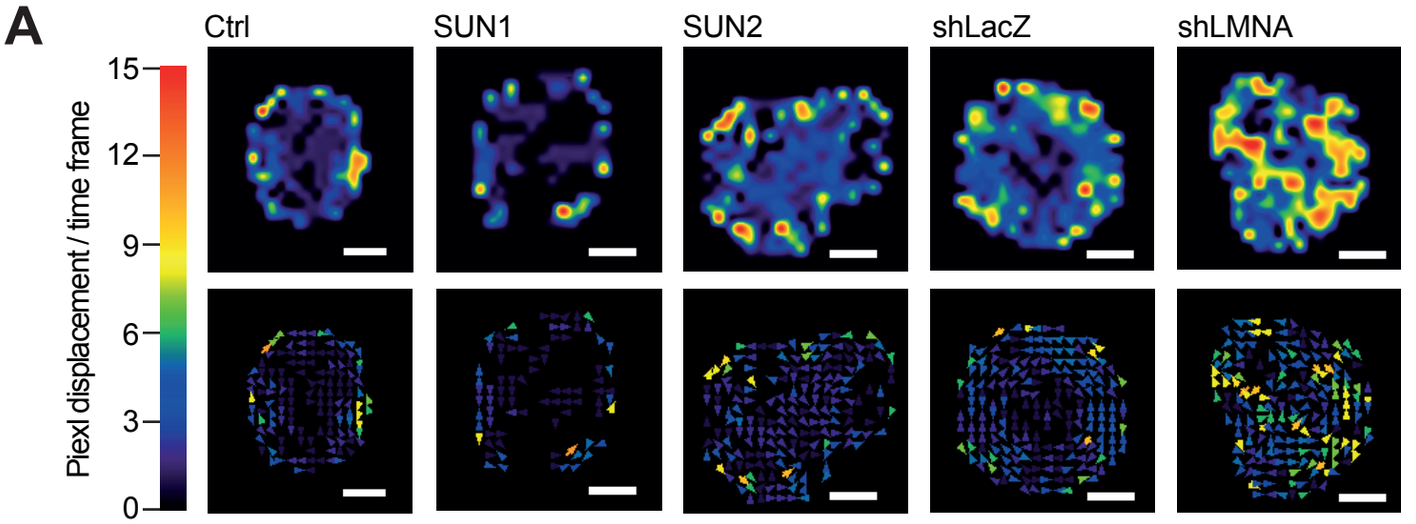
A
Ctrl
SUN1
SUN2
shLacZ
shLMNA
Piexl displacement / time frame
15
12
9
6
3
0

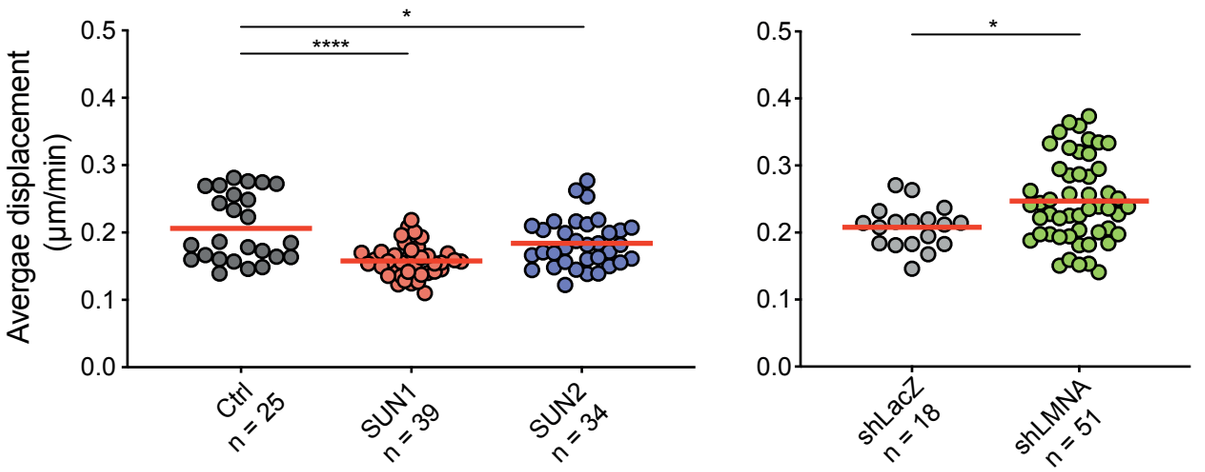
B
Avergae displacement (µm/min)
0.5
0.4
0.3
0.2
0.1
0.0
*
****
Ctrl n = 25
SUN1 n = 39
SUN2 n = 34
shLacZ n = 18
shLMNA n = 51

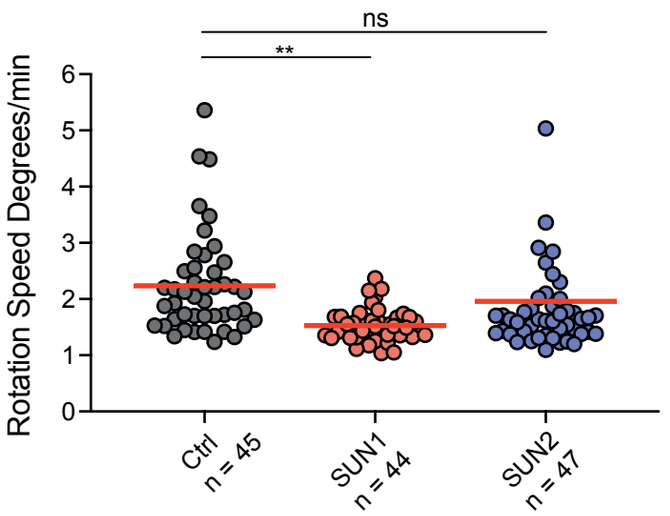
C
Rotation Speed Degrees/min
6
5
4
3
2
1
0
ns
**
Ctrl n = 45
SUN1 n = 44
SUN2 n = 47

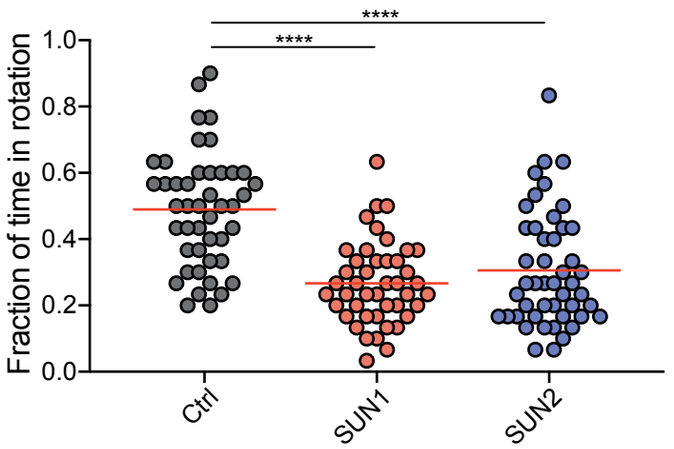
Fraction of time in rotation
1.0
0.8
0.6
0.4
0.2
0.0
****
****
Ctrl
SUN1
SUN2

Figure S1

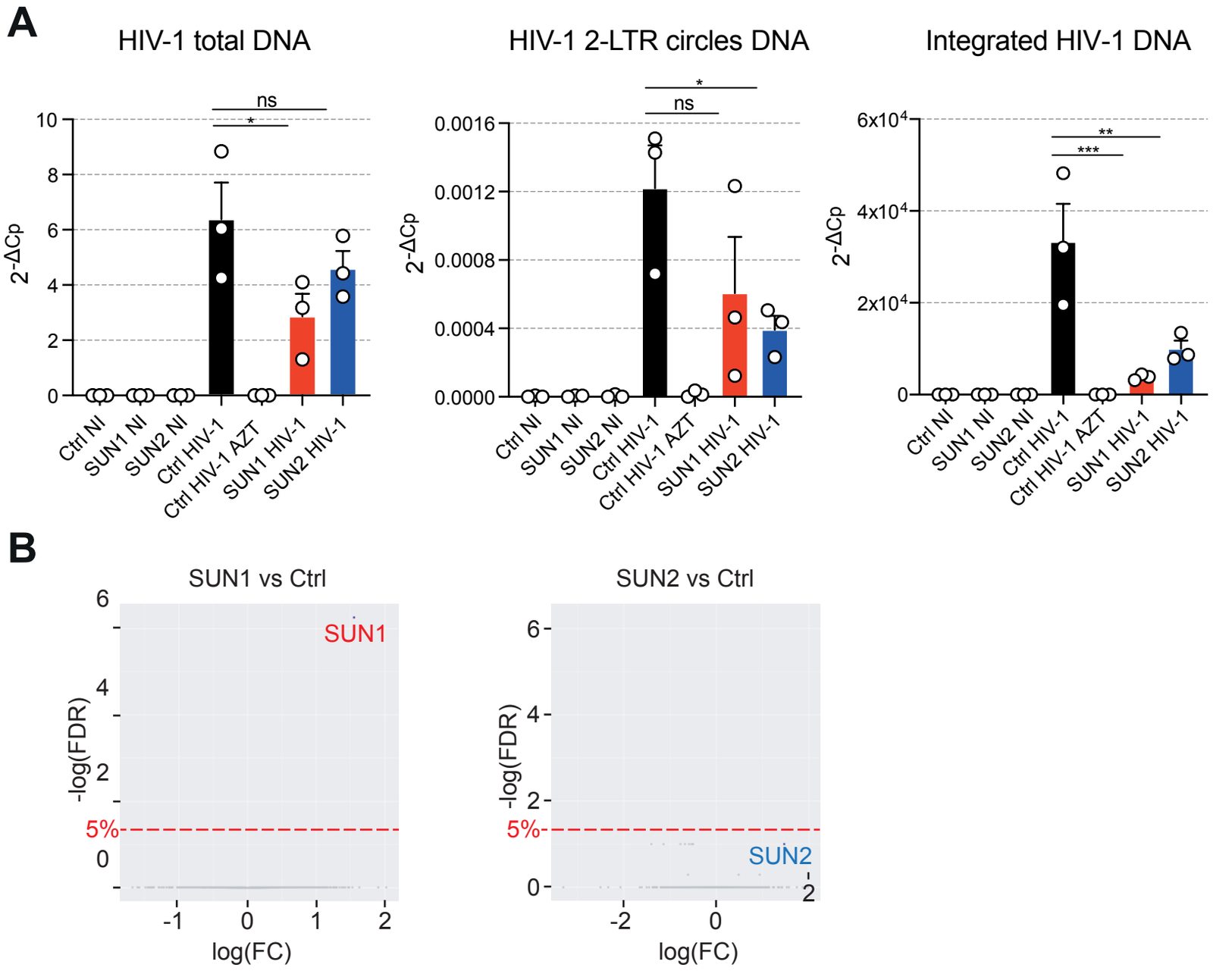
A
HIV-1 total DNA
HIV-1 2-LTR circles DNA
Integrated HIV-1 DNA
2-ΔCp
ns
*
**
***
Ctrl NI
SUN1 NI
SUN2 NI
Ctrl HIV-1
Ctrl HIV-1 AZT
SUN1 HIV-1
SUN2 HIV-1
B
SUN1 vs Ctrl
SUN2 vs Ctrl
-log(FDR)
log(FC)
5%
SUN1
SUN2

Figure S2

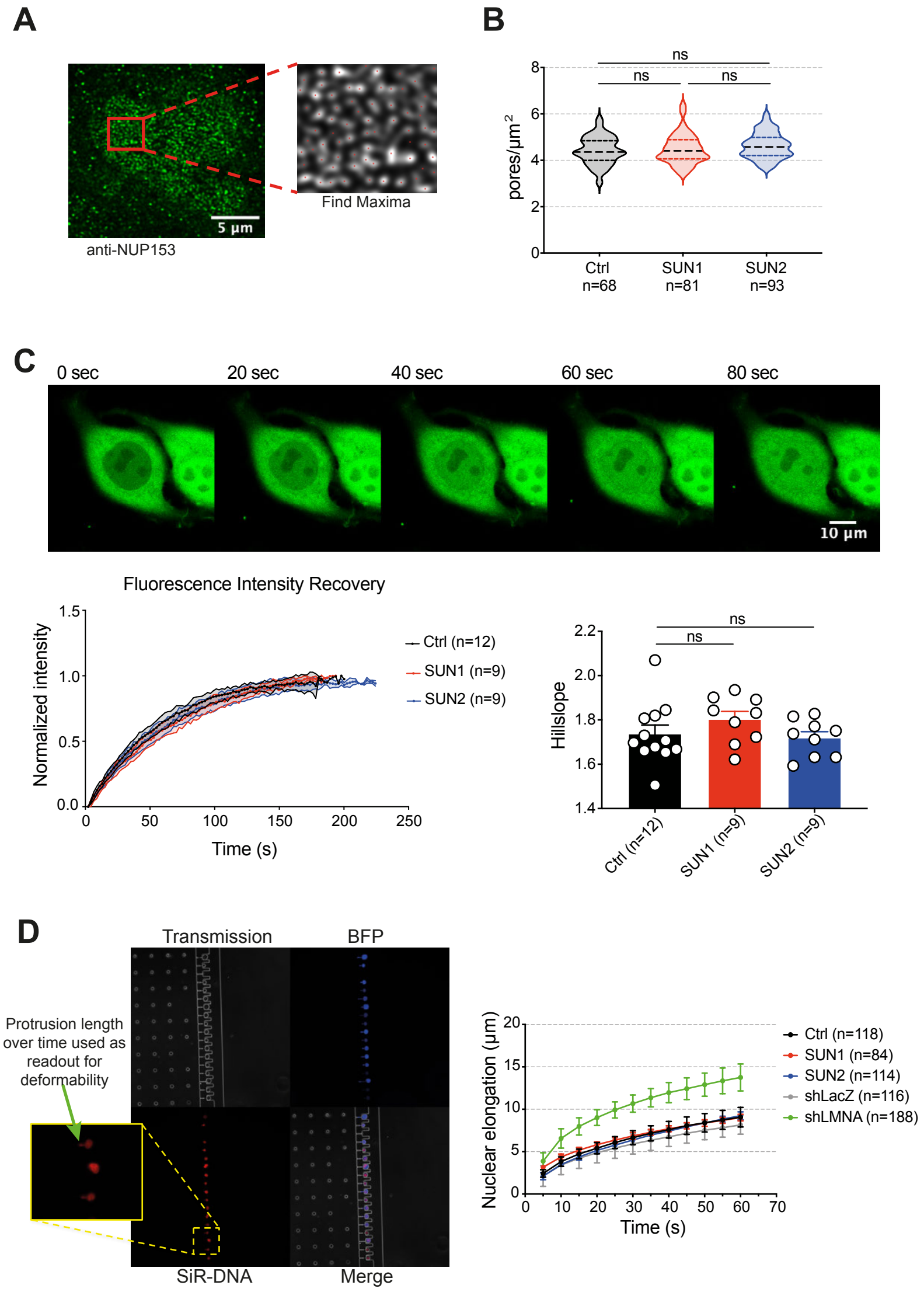
A
5 µm
anti-NUP153
Find Maxima
B
ns
ns
ns
pores/µm²
8
6
4
2
0
Ctrl
n=68
SUN1
n=81
SUN2
n=93
C
0 sec
20 sec
40 sec
60 sec
80 sec
10 µm
Fluorescence Intensity Recovery
Normalized intensity
1.5
1.0
0.5
0.0
0
50
100
150
200
250
Time (s)
Ctrl (n=12)
SUN1 (n=9)
SUN2 (n=9)
Hillslope
2.2
2.0
1.8
1.6
1.4
ns
ns
Ctrl (n=12)
SUN1 (n=9)
SUN2 (n=9)
D
Transmission
BFP
Protrusion length over time used as readout for deformability
SiR-DNA
Merge
Nuclear elongation (µm)
20
15
10
5
0
0
10
20
30
40
50
60
70
Time (s)
Ctrl (n=118)
SUN1 (n=84)
SUN2 (n=114)
shLacZ (n=116)
shLMNA (n=188)

Figure S3

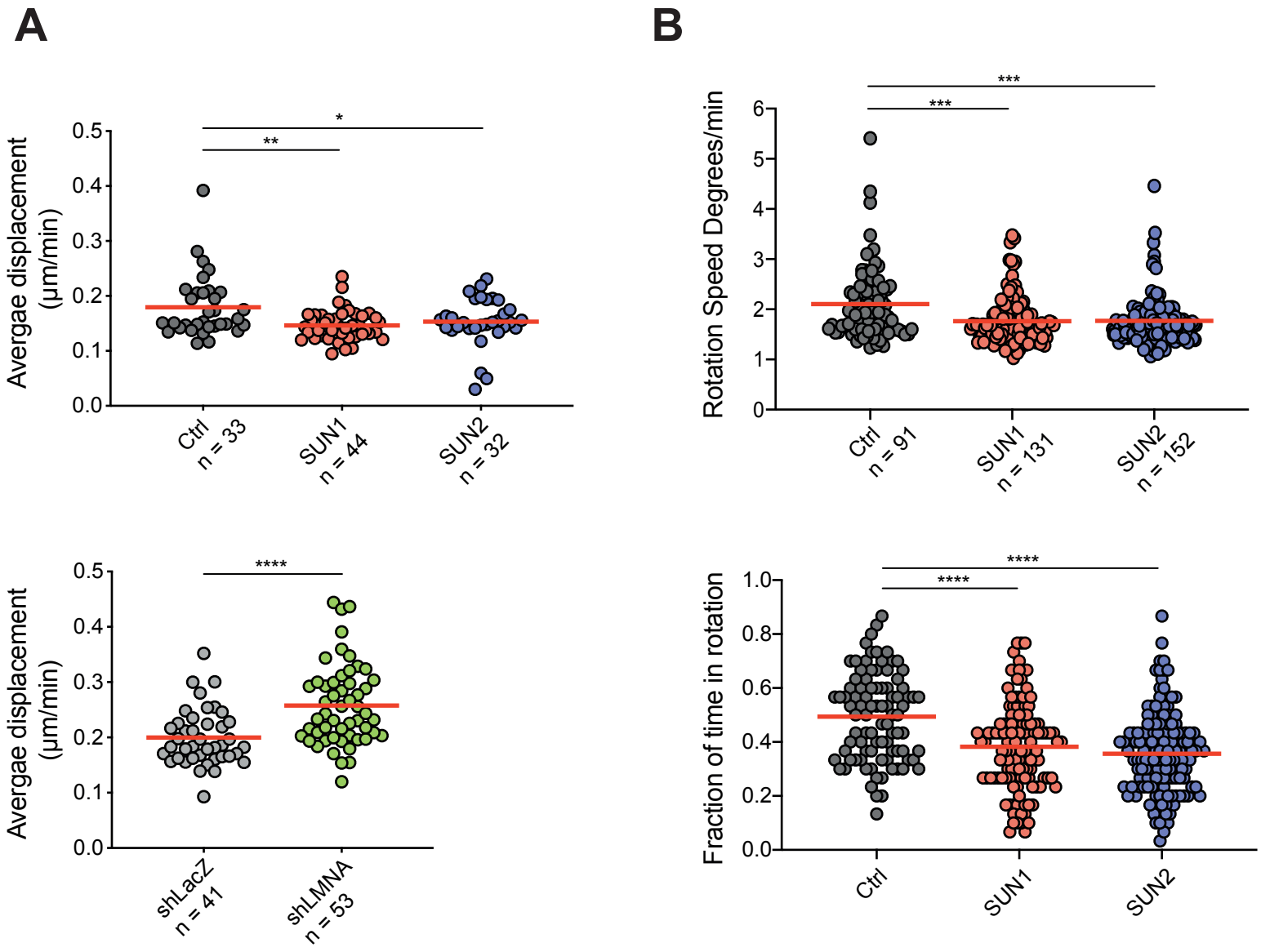
A
B
Avergae displacement (µm/min)
0.5
0.4
0.3
0.2
0.1
0.0
*
**
Ctrl n = 33
SUN1 n = 44
SUN2 n = 32
Rotation Speed Degrees/min
6
5
4
3
2
1
0
***
***
Ctrl n = 91
SUN1 n = 131
SUN2 n = 152
Avergae displacement (µm/min)
****
shLacZ n = 41
shLMNA n = 53
Fraction of time in rotation
1.0
0.8
0.6
0.4
0.2
0.0
****
****
Ctrl
SUN1
SUN2